The Cryosphere, 15, 5261–5280, 2021
https://doi.org/10.5194/tc-15-5261-2021


The Cryosphere Open Access EGU

# Spatiotemporal distribution of seasonal snow water equivalent in High Mountain Asia from an 18-year Landsat–MODIS era snow reanalysis dataset

**Yufei Liu, Yiwen Fang, and Steven A. Margulis**

Department of Civil and Environmental Engineering, University of California, Los Angeles, Los Angeles, CA, USA

**Correspondence:** Steven A. Margulis (margulis@seas.ucla.edu)

Received: 9 May 2021 – Discussion started: 17 May 2021
Revised: 4 October 2021 – Accepted: 19 October 2021 – Published: 26 November 2021

**Abstract.** Seasonal snowpack is an essential component in the hydrological cycle and plays a significant role in supplying water resources to downstream users. Yet the snow water equivalent (SWE) in seasonal snowpacks, and its space–time variation, remains highly uncertain, especially over mountainous areas with complex terrain and sparse observations, such as in High Mountain Asia (HMA). In this work, we assessed the spatiotemporal distribution of seasonal SWE, obtained from a new 18-year HMA Snow Reanalysis (HMASR) dataset, as part of the recent NASA High Mountain Asia Team (HiMAT) effort. A Bayesian snow reanalysis scheme previously developed to assimilate satellite-derived fractional snow-covered area (fSCA) products from Landsat and MODIS platforms has been applied to develop the HMASR dataset (at a spatial resolution of 16 arcsec (∼ 500 m) and daily temporal resolution) over the joint Landsat–MODIS period covering water years (WYs) 2000–2017.

Based on the results, the HMA-wide total SWE volume is found to be around 163 $km^3$ on average and ranges from 114 $km^3$ (WY2001) to 227 $km^3$ (WY2005) when assessed over 18 WYs. The most abundant snowpacks are found in the northwestern basins (e.g., Indus, Syr Darya and Amu Darya) that are mainly affected by the westerlies, accounting for around 66 % of total seasonal SWE volume. Seasonal snowpack in HMA is depicted by snow accumulating through October to March and April, typically peaking around April and depleting in July–October, with variations across basins and WYs. When examining the elevational distribution over the HMA domain, seasonal SWE volume peaks at mid-elevations (around 3500 m), with over 50 % of the volume stored above 3500 m. Above-average amounts of precipitation causes significant overall increase in SWE volumes across all elevations, while an increase in air temperature (∼ 1.5 K) from cooler to normal conditions leads to an redistribution in snow storage from lower elevations to mid-elevations.

This work brings new insight into understanding the climatology and variability of seasonal snowpack over HMA, with the regional snow reanalysis constrained by remote-sensing data, providing a new reference dataset for future studies of seasonal snow and how it contributes to the water cycle and climate over the HMA region.

## 1 Introduction

The High Mountain Asia (HMA) region consists of the major mountain ranges and headwaters of the largest rivers in Asia. It features extremely high elevation, complex topography, and significant glacier and snow cover. In HMA, glacier melt and snowmelt are vital to the hydrological cycle and water supply, as they feed the major regional rivers with over one billion people living downstream (Barnett et al., 2005; Bookhagen and Burbank, 2010; Immerzeel et al., 2010, 2020; Immerzeel and Bierkens, 2012; Lutz et al., 2014; Armstrong et al., 2019; Scott et al., 2019).

Even though both seasonal snow and glaciers are crucial to hydrology and water availability, seasonal snow has arguably received less attention than glaciers in the HMA region. Many studies have addressed the status and changes in glaciers over HMA (e.g., Bolch et al., 2012, 2019; Kääb et al., 2012; Sorg et al., 2012; Yao et al., 2012; Lutz et al., 2014; Rounce et al., 2020; Shean et al., 2020). For seasonal snow,

previous studies have examined the snow extent (e.g., Dahe et al., 2006; Pu et al., 2007; Immerzeel et al., 2009; Tahir et al., 2011; Basang et al., 2017; Wang et al., 2017; Notarnicola, 2020) or snow mass and snow depth (e.g., Dahe et al., 2006; Che et al., 2008; Terzago et al., 2014; Dai et al., 2017; Stigter et al., 2017; Smith and Bookhagen, 2018, 2020; Ahmad et al., 2019; Kirkham et al., 2019; Xue et al., 2019; Bair et al., 2018, 2020, 2021). In the current literature involving seasonal snow, most of the studies have focused on snow-covered area (or extent, which is readily available from satellite-borne remote sensing) instead of snow mass or have been applied at relatively localized scales (e.g., individual small to moderate sized basins) or coarse scales (e.g., above 1 km) over larger scales. The seasonal snow water storage and its spatiotemporal distribution across HMA are highly uncertain, primarily due to the lack of in situ observations and fine-scale (e.g., $< 1$ km) snow water equivalent (SWE) datasets over this large domain (Takala et al., 2011; Kirkham et al., 2019). In fact, accurately estimating SWE at such scales remains a great challenge worldwide, and it is even more difficult in mountainous regions due to the terrain complexity (Lettenmaier et al., 2015; Dozier et al., 2016; Bormann et al., 2018).

In situ measurements are usually expensive and difficult to install and maintain in HMA and are mostly located in low-lying valleys, thus resulting in a sparse and potentially non-representative network (Winiger et al., 2005; Palazzi et al., 2013; Dozier et al., 2016; Kirkham et al., 2019). In recent decades, satellite observations can provide large-scale estimates of some snowpack properties. However, most of these measured properties, such as snow-covered area (SCA) based on visible and near-infrared bands (e.g., Dozier, 1989; Hall et al., 2002; Painter et al., 2009), are only indirectly related to snow mass. While SWE and snow depth can be directly estimated from passive microwave sensors (using retrieval algorithms based on the brightness temperature; e.g., Chang et al., 1987), these estimates are at coarse spatial resolution (e.g., 25 km) and are generally negatively biased in deep snowpacks (Takala et al., 2011; Dozier et al., 2016). Recent applications of C-band synthetic aperture radar (SAR) techniques show promise for snow depth retrieval (Lievens et al., 2019) but are available only over recent years and do not directly provide SWE.

Global atmospheric reanalysis products provide another approach to large-scale SWE estimates as by-products of their land surface schemes. Examples include the Global Land Data Assimilation System (GLDAS, Rodell et al., 2004), Modern-Era Retrospective analysis for Research and Applications (MERRA, Rienecker et al., 2011; MERRA-2, Gelaro et al., 2017), European Centre for Medium-Range Weather Forecasts (ECMWF) reanalysis products (ERA-Interim, Dee et al., 2011; ERA5, Hersbach et al., 2020), High Asia Refined analysis (HAR, Maussion et al., 2011, 2014), Japanese 55-year Reanalysis (JRA-55; Kobayashi et al., 2015), and others. SWE estimates in these datasets are found to be generally consistent in their interannual and seasonal variations but can differ significantly in their magnitudes when evaluated over different regions (Mudryk et al., 2015; Wrzesien et al., 2019), where the uncertainties come from different land surface models and meteorological inputs (Mudryk et al., 2015; Mortimer et al., 2020; Kim et al., 2021). In addition, most reanalysis datasets are not specifically designed for SWE estimation, and only a few of them (e.g., ERA5 and JRA55) assimilate snow observations (including in situ and remote sensing) in HMA. Bian et al. (2019) found many reanalysis datasets overestimate SWE compared to ground observations in the Tibetan Plateau, although part of the differences may come from inconsistent spatial resolution and elevations between in situ and gridded datasets. The performance of these large-scale reanalysis datasets over the full HMA domain has not been fully assessed due to the sparse and uneven in situ station network.

Recent works have contributed to the development of SWE (or snow depth) estimates covering the HMA region based on passive microwave (e.g., Talaka et al., 2011; Smith and Bookhagen, 2016; Dai et al., 2017; Pulliainen et al., 2020) or active microwave measurements (Lievens et al., 2019), with machine-learning approaches employed to improve the accuracy in SWE estimation (e.g., Ahmad et al., 2019). Alternatively, satellite-observed snow-covered area products can also provide valuable information in SWE estimation. For example, fractional snow-covered area (fSCA) products are used in SWE reconstruction methods to improve the estimates of SWE over Indus and Amu Darya, by calculating snowmelt backward from melt-out to peak SWE timing using satellite-observed snow disappearance rates (Bair et al., 2018, 2020). In addition, data assimilation (DA) approaches that explicitly merged snow observations with modeling are effective in providing more realistic SWE estimates and reducing SWE uncertainties especially over the mountains (Xue et al., 2019; Largeron et al., 2020): both JRA-55 and ERA5 products assimilate ground snow depth and satellite-retrieved snow cover observations; GlobSnow (Talaka et al., 2011; Pulliainen et al., 2020) products assimilate passive-microwave-retrieved SWE along with ground snow depth observations to provide SWE and snow extent estimates, while mountain areas with high terrain complexity are masked out. These are promising approaches to improve the accuracy in SWE estimates over HMA, yet currently there is still a need for large-scale SWE datasets at higher resolution, over a longer period and covering mountainous areas in this region.

To better understand the spatiotemporal pattern and variability in seasonal snowpack over HMA, the so-called High Mountain Asia Snow Reanalysis (HMASR; Liu et al., 2021) dataset is used herein to characterize the seasonal snow climatology and variability over HMA. The dataset covers the joint Landsat–MODIS era between water years (WYs) 2000 to 2017 (which will be extended to present in later versions) and was developed as part of the NASA High Moun-

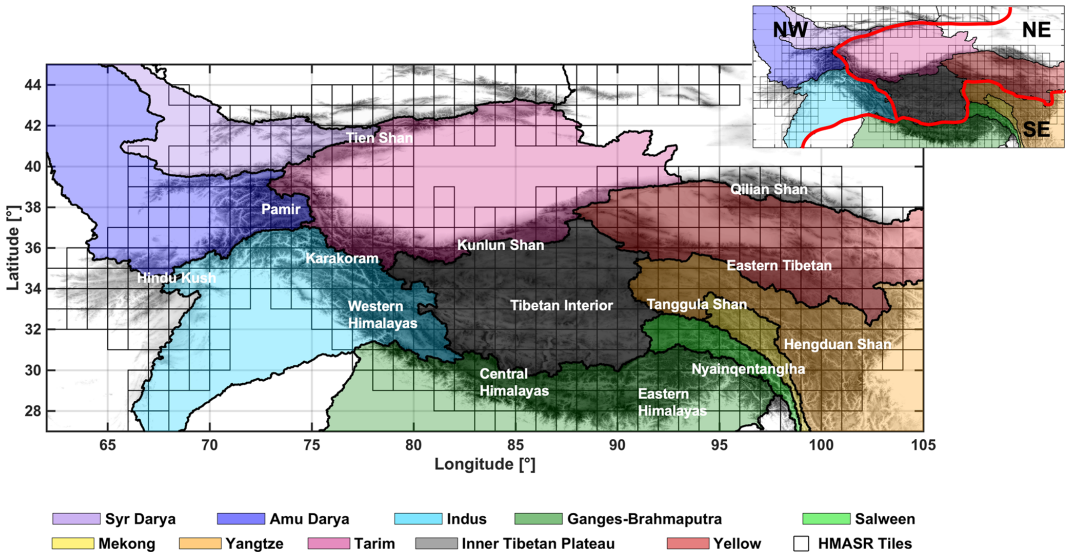


**Figure 1.** Map of HMA domain with HMASR tiles marked with black boxes. Major watersheds are delineated and colored on the map based on HydroSHEDS (Lehner et al., 2008). Major mountain ranges are labeled with reference to Bolch et al. (2019). A division of the HMA domain into northwestern (NW), northeastern (NE) and southeastern (SE) subregions, which are used for descriptive purposes in this study, is shown in the inset.

tain Asia Team (HiMAT) activities. HiMAT is a multi-investigator effort in developing new datasets to understand cryosphere variability over HMA (Osmanoglu et al., 2017). The HMASR dataset provides daily estimates of SWE, fSCA and other snow variables, at a 16 arcsec ($\sim$ 500 m) resolution. SWE estimates are derived by assimilating fSCA from Landsat and MODIS platforms using a previously developed snow reanalysis framework (Margulis et al., 2019), where the method has been shown in previous applications to provide realistic SWE estimates over mountainous domains in the Sierra Nevada (Margulis et al., 2016) and Andes (Cortés and Margulis, 2017). The HMASR aims to fill the spatiotemporal gaps in existing SWE datasets and allow for better characterization of the distribution and changes in seasonal snow storage, as well as provide insights into the hydrologic cycle and water availability over HMA. Using this dataset, the spatial distribution of SWE climatology is examined at annual and seasonal scales over the HMA region, covering the highest mountain ranges and the Tibetan Plateau in Asia. Integrated SWE volumes over the full HMA domain and over the major river basins (e.g., Syr Darya, Amu Darya, Indus, Ganges–Brahmaputra, Yangtze and Yellow), and their variation with elevation, are also quantified in this work. The following scientific questions are addressed herein:

1. How is seasonal snow distributed spatially across the major watersheds of HMA?
2. What is the seasonal and interannual variability in amount of snow storage over HMA?
3. How is the amount of snow distributed across elevation, and how does it vary under different climate conditions?

## 2 Data and method

This section describes the data and methods used in this study. Section 2.1 introduces the study domain, including the major river basins and mountain ranges in the region. Section 2.2 and 2.3 provide a brief description of the reanalysis method, input data and models used in the development of the HMASR. Finally, a non-seasonal snow and ice mask applied to mask out semi-permanent snow and ice for the assessment of seasonal snow is explained in Sect. 2.4.

### 2.1 HMA domain

The HMA domain used in this work is bounded from 27 to 45° N and from 60 to 105° E (Fig. 1), covering the highest mountain ranges and plateaus (the Tien Shan, Pamir Mountains, Hindu Kush, Karakoram, Himalayas and Tibetan Plateau), as well as the headwaters of the main river basins (Syr Darya, Amu Darya, Indus, Ganges–Brahmaputra, Yangtze and Yellow). Winter westerlies and the summer monsoon are the major moisture sources in this region, significantly influencing the spatiotemporal patterns in snowfall and glacier mass balance. More specifically, the northern and western HMA is dominated by westerlies and receives abundant winter snowfall, while the southern and eastern HMA is dominated by the Indian monsoon from June to September and receives a considerable amount of summer snowfall; the eastern edges of HMA are affected by the East Asia monsoon but with limited impact (Bookhagen and Burbank, 2010; Yao et al., 2012; Bolch et al., 2019). Note that in HMASR, outputs are provided for each regular 1° by 1° latitude–longitude tile (within which a regular computational

grid of 16 arcsec is used), and tiles with a tile-averaged elevation above 1500 m were selected and processed in the dataset (Fig. 1). This tile-average threshold (1500 m) was chosen conservatively to capture the vast majority of seasonal mountain snow over HMA, avoid running a large number of tiles with negligible snow and reduce the computational load in product development. We acknowledge this threshold might exclude snow in some areas of the domain (e.g., northern HMA) and anticipate this threshold to be relaxed or removed in future versions of this product.

For convenience in presenting results herein, the HMA domain was divided into three large subregions, namely the northwestern (NW), southeastern (SE) and northeastern (NE) subregions (Fig. 1). Major river basins are identified in each subregion, namely those located in the NW (Syr Darya, Amu Darya and Indus), SE (Ganges–Brahmaputra, Salween, Mekong and Yangtze) and NE (Tarim, Inner Tibetan Plateau and Yellow) subregions. Similarly, the major mountain ranges are also identified in each subregion, namely those located in the NW (e.g., the Tien Shan, Pamir Mountains, Hindu Kush, Karakoram and western Himalayas), SE (e.g., central and eastern Himalayas, Nyainqêntanglha Mountains, Tanggula Shan and Hengduan Shan) and NE (e.g., Kunlun Shan, Tibetan Interior, eastern Tibetan mountains and Qilian Shan) subregions and are labeled in Fig. 1.

### 2.2 Snow reanalysis scheme

A previously developed snow reanalysis methodology (Margulis et al., 2019) is employed in deriving the HMASR. For brevity, only the key details are repeated here. Prior model estimates are obtained via the coupled Simplified Simple Biosphere model, version 3 (SSiB3; Sun and Xue, 2001; Xue et al., 2003) and the Liston (2004) snow depletion curve (SDC). The SSiB3 model is used as the land surface model (LSM) in this work, which has three snow layers with vegetation canopy and soil representations. It requires hourly inputs of forcing data (e.g., precipitation, air temperature, radiation, wind speed, humidity and pressure) and static inputs (e.g., topography, land cover, vegetation and soil type), with more details clarified in Sect. 2.3.1. The SSiB3 model provides the basic mass and energy fluxes for the snowpack based on meteorological inputs and physiographic characteristics. These fluxes are used with the Liston SDC to derive estimates of grid-averaged SWE and fSCA. Specifically, the Liston SDC assumes that the subgrid distribution of SWE follows a log-normal distribution and is a function of grid-averaged SWE, melt and a parameter of subgrid coefficient of variation. The SDC yields the prediction of fSCA that is compared with satellite-observed fSCA and serves as the constraint in the data assimilation.

As done in many data assimilation methods, an ensemble approach is used in the snow reanalysis scheme, whereby the model generates prior estimates of snow states (i.e., SWE, snow depth, fSCA, etc.) with postulated uncertainties. Meteorological forcing inputs are bias-corrected, downscaled to the modeling grid (16 arcsec) and perturbed with uncertainty in the ensemble approach, using the methods described in Durand et al. (2008) and Girotto et al. (2014). To constrain the prior snow estimates on the remotely sensed fSCA observations, a Bayesian update is performed using the particle batch smoother (PBS; Margulis et al., 2015, 2019) approach. Posterior snow estimates are obtained in this update step by more heavily weighting ensemble members that are more consistent with the batch of observed fSCA in a given water year using a Bayesian likelihood function that accounts for model–measurement misfit and measurement error. It is worthwhile to note that the posterior ensemble mean, median and spread (or other statistics) can be obtained via the Bayesian update step. Herein, the posterior ensemble median values of SWE are described when assessing the SWE over HMA. Details of the PBS methods are described in Margulis et al. (2015, 2019), and more details on fSCA observations are provided in Sect. 2.3.2.

The lack of in situ SWE data over HMA prevents a thorough verification of the HMASR. However, previous applications of the snow reanalysis method in similarly complex terrain in the Sierra Nevada of the Western US and the South American central Andes thoroughly compared reanalysis estimates vs. in situ and airborne-derived SWE data. Performance in both domains was positive relative to in situ data with values of mean error, root-mean-squared error and correlation coefficients of $\sim 3$ cm, 13 cm and 0.95 for the Sierra Nevada (Margulis et al., 2016) and $\sim 1$ cm, 29 cm and 0.73 for the Andes (Cortés and Margulis, 2017), respectively. In Margulis et al. (2019), comparison with the Airborne Snow Observatory (ASO) SWE data in Tuolumne in the Sierra Nevada yielded similar results (mean error, root-mean-squared error and correlation coefficients of $\sim 5$ cm, 23 cm and 0.84). Here we provide the caveat that performance of the method may be degraded in parts of the HMA region due to the frequent cloud-obscuring issues (see more details in Sect. 2.3.2), compared to previous work in the Sierra Nevada or Andes.

### 2.3 Input data acquisition and processing

#### 2.3.1 Meteorological, topographic and land cover data

In HMASR, the prior surface meteorological inputs were obtained from MERRA-2 (Global Modeling and Assimilation Office (GMAO), 2015a, b, c; MERRA-2 tavg1_2d_flx_Nx; MERRA-2 tavg1_2d_rad_Nx; MERRA-2 tavg1_2d_slv_Nx) at its raw resolution (0.5° by 0.625° latitude–longitude), including precipitation, air temperature, solar radiation, specific humidity, surface pressure and wind speed. The uncertainty models and their parameters used to perform bias correction and uncertainty perturbation are specified in Margulis et al. (2019) for the HMA region, ex-

cept that prior ensemble precipitation is perturbed by a log-normal distribution with mean of 1.54 and coefficient of variation (CV) of 0.83 based on the results from Liu and Margulis (2019).

Digital elevation model (DEM) data were obtained from the Shuttle Radar Topography Mission (SRTM, http://www2.jpl.nasa.gov/srtm/, last access: 28 March 2018) 1 arcsec product and aggregated to 16 arcsec ($\sim$ 500 m) resolution. Gaps in DEM data were filled by the Advanced Spaceborne Thermal Emission and Reflection Radiometer (ASTER) Global Digital Elevation Model (GDEM, version 2) 1 arcsec product (https://asterweb.jpl.nasa.gov/, last access: 3 April 2018). Land cover data were obtained from the Advanced Very High Resolution Radiometer (AVHRR) global land cover classification dataset (Hansen et al., 2000). Forest cover information was obtained from the tree canopy cover (TCC) product containing the Landsat Vegetation Continuous Fields (https://lcluc.umd.edu/metadata/global-30m-landsat-tree-canopy-version-4, last access: 29 March 2018; Sexton et al., 2013).

### 2.3.2 fSCA data

The fSCA observations used to condition prior snow estimates were retrieved from Landsat (https://www.usgs.gov/land-resources/nli/landsat/data-tools; last access: 1 October 2019) and MODIS platforms, for their joint period of WYs 2000 to 2017 (e.g., where WY2000 corresponds to 1 October 1999–30 September 2000). The (nadir-viewing) Landsat-based fSCA data were obtained from Landsat 5, 7 and 8 satellites, retrieved using a spectral unmixing algorithm (Painter et al., 2003; Cortés et al., 2014), available at 30 m and every 16 d (excluding cloudy days). The (nadir- and off-nadir-viewing) MODIS-based fSCA data were obtained from the MODIS snow-covered area and grain size (MODSCAG, https://snow.jpl.nasa.gov/portal/data/; last access: 26 February 2019) product (Painter et al., 2009), available daily at 500 m, with a viewing angle between 0 and 55°. Jointly assimilating fSCA from both platforms provides more measurements to compensate for cloud contamination in HMA.

Cloud screening and viewing angle screening were performed as illustrated in Margulis et al. (2019), and here we only clarify the key steps for brevity. Specifically, for Landsat, any image with a diagnosed cloud cover fraction of greater than 40 % is excluded entirely. For MODSCAG, only near-nadir pixels within an image are included, and, of those, any image with a diagnosed cloud cover fraction of greater than 10 % is excluded entirely. This subset of Landsat and MODSCAG images for inclusion therefore uses a conservative screening meant to exclude significantly cloud-contaminated tiles. This does not prevent errors of omission/commission in cloud/snow identification but is meant to mitigate cloud impacts by not including those deemed significantly cloudy. It should also be noted that the snow reanalysis method used herein is less susceptible to errors of omission/commission when compared to SWE reconstruction methods (e.g., Bair et al., 2020) that interpolate between fSCA measurements to estimate ablation rates. Instead, the snow reanalysis fitting of fSCA measurements is more akin to a least-squares type fit where measurement errors are accounted for in the framework. This mitigates the propagation of errors of omission/commission compared to SWE reconstruction techniques. For images that passed through the cloud/viewing angle screening, cloudy pixels within each image were further excluded through internal cloud masks. After screening, both Landsat and MODSCAG images were aggregated to the same modeling resolution (16 arcsec).

No large systematic differences were seen when examining fSCA across different Landsat sensors, while substantial differences were found in same-day fSCA images between Landsat and MODSCAG (after screening and aggregation). To reconcile the inconsistency between products, a cumulative distribution function (CDF)-matching method was applied pixel-wise to statistically match MODSCAG images with Landsat images. Based on the analysis in Margulis et al. (2019), we specify a measurement error standard deviation (10 % of Landsat fSCA; 15 % of CDF-matched MODSCAG fSCA) in the reanalysis to represent retrieval error/uncertainty.

It is worthwhile to note that the fSCA data availability is significantly affected by cloud contamination in some areas of the HMA region, especially during the monsoon season (June–September) where fSCA measurements are limited over regions such as the Himalayas (Fig. 2). The lack of abundant fSCA data can be a potential limitation in assimilating fSCA observations for these monsoon-affected regions and therefore leads to higher uncertainty and less constrained posterior SWE estimates (i.e., where in the limit of no available observations, the posterior will, by construct, equal the prior estimate).

## 2.4 Non-seasonal snow and ice mask

A significant fraction of HMA is covered by glacier or semi-permanent snow owing to its extremely high elevation. Thus, it is important to distinguish seasonal vs. non-seasonal snow over land or glacier surfaces. In particular, the reanalysis method used in the development of the HMASR is best suited for seasonal snow characterization, because it relies on the signal between fSCA depletion time series and SWE via the LSM–SDC model. Hence, those pixels where there is not a full melt-out of snow are expected to be potentially erroneous. So, while estimates are generated at all pixels in the domain, the aim to focus on seasonal snow requires masking out semi-permanent snow and ice. Glacier inventories from the Global Land Ice Measurements from Space (GLIMS; Raup et al., 2007) and the Randolph Glacier Inventory (RGI; Pfeffer et al., 2014; RGI Consortium, 2017) have been employed in previous studies to exclude glaciers from

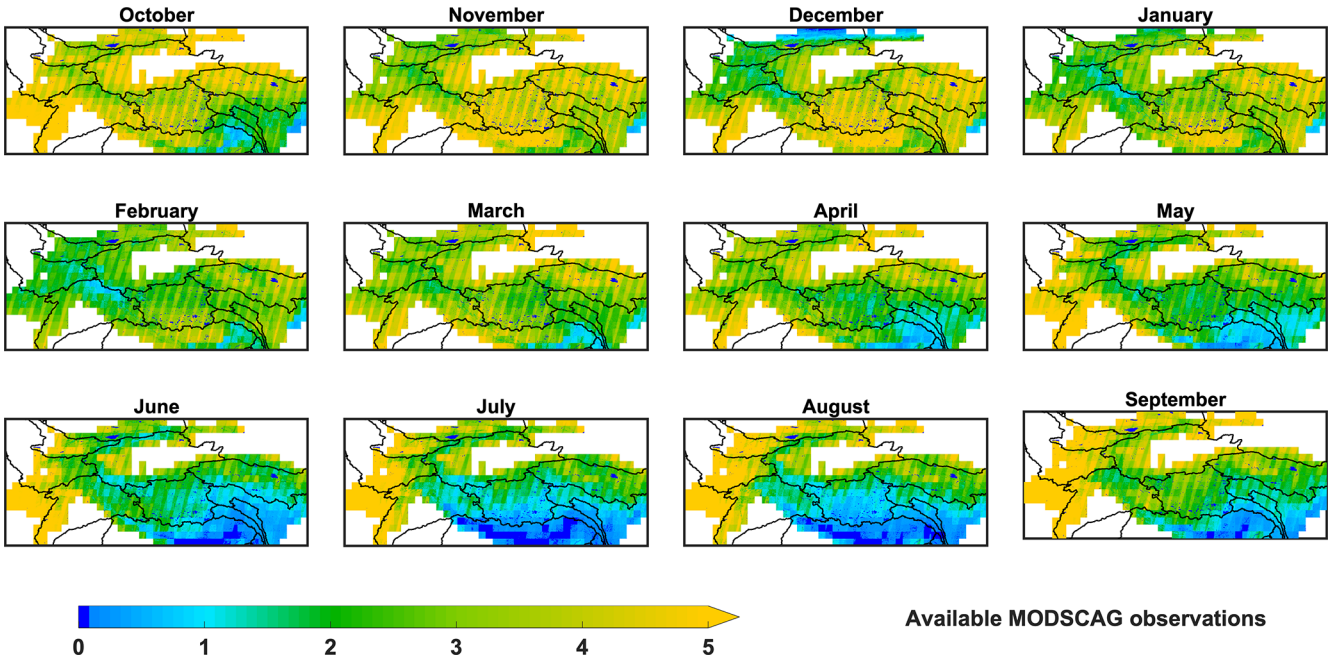


**Figure 2.** Monthly total number of available (near-nadir) MODSCAG measurements averaged over 18 years, with cloud and viewing angle screening. Landsat measurements supplement these MODIS-derived measurements. The dark blue color is used to distinguish pixels with zero MODSCAG measurements.

snow modeling domains (e.g., Wrzesien et al., 2019; Smith and Bookhagen, 2018). Other studies such as Mudryk et al. (2015) and Mortimer et al. (2020) excluded glaciers based on estimates from the MERRA land fraction mask. Armstrong et al. (2019) applied the MODIS Persistent Ice (MODICE; Painter et al., 2012) algorithm to derive a minimum snow and ice mask based on the MODSCAG product and used it to distinguish seasonal snow from glaciers or persistent snow.

Herein a combination method was used to exclude the non-seasonal snow and ice pixels in HMASR, based on (1) a glacier mask derived from GLIMS to identify glacierized pixels and (2) a persistent snow mask derived from the HMASR dataset itself. We acknowledge that RGI dataset may be more appropriate to use than GLIMS, as it obtains glacier outlines around 2000 while GLIMS obtains those from a larger date range. To be more specific on the second mask, pixels with a significant amount of persistent snow were identified by comparing the annual minimum SWE at a particular pixel to its annual maximum SWE in each year. If the minimum SWE exceeds 10 % of the maximum SWE for more than once out of the 18 years, the pixel is considered to be a persistent snow pixel to be masked out in the computation of seasonal snow estimates. The derived glacier and persistent snow masks are combined into a non-seasonal snow and ice mask, which is applied when presenting the spatiotemporal patterns of seasonal SWE in the following section.

## 3 Results and discussion

The HMASR dataset is designed to provide a reliable and consistent SWE product that can be used for assessing the spatiotemporal distribution of seasonal SWE over the recent remote-sensing record. To present an overall assessment of seasonal snowpack variability in the HMA region using the HMASR dataset, the results are organized as follows: (1) the spatial distribution of seasonal snowpack climatology, at annual peak and seasonal scales; (2) the temporal distribution of seasonal snowpack volume at basin and domain-wide scales; and (3) the elevational distribution of seasonal snowpack storage at HMA-wide and basin scales.

### 3.1 Spatial distribution of seasonal SWE climatology

The spatial distribution of SWE is valuable in assessing the regional water storage. Given the strong seasonal signature of snowpack processes over much of the domain, the pixel-wise peak SWE is a useful metric to quantify the distribution of the maximum amount of snow water mass held in the seasonal snowpack within a given water year. Hence, the spatial distribution of peak SWE (Sect. 3.1.1) and the associated timing (Sect. 3.1.2) are examined in this section, with seasonal evolution of SWE averaged over fall, winter, spring and summer also assessed (Sect. 3.1.3).

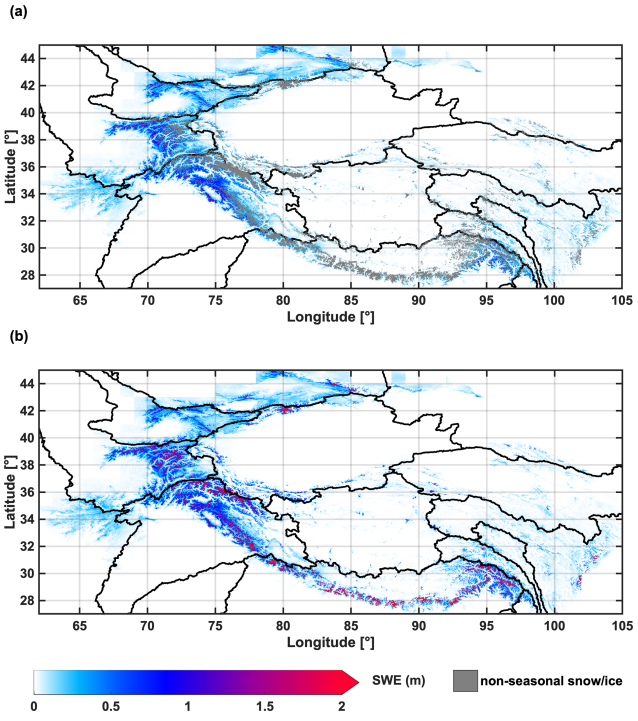


**Figure 3.** **(a)** Map of pixel-wise peak seasonal SWE climatology, with non-seasonal snow and ice pixels masked out (gray). **(b)** Map of pixel-wise peak seasonal SWE climatology, without masking of non-seasonal snow and ice pixels for reference.

### 3.1.1 Peak seasonal SWE climatology

The climatology (18-year average) of pixel-wise peak SWE over the HMA region is depicted in Fig. 3, where Fig. 3a presents only the results for seasonal snow pixels (where non-seasonal snow and ice pixels have been masked out). Figure 3b presents the results for all pixels for illustration (where significantly higher amounts of SWE show up in non-seasonal snow and ice mask pixels, corresponding to glaciers or permanent snow), where the non-seasonal snow mask covers $\sim 4.7\,\%$ of the domain area. The non-seasonal SWE values (Fig. 3b) are expected to be unreliable because the initial conditions for SWE at those locations at the beginning of the dataset are unknown and the lack of full melt-out makes the relationship between fSCA depletion and peak SWE much less direct.

In general, seasonal snow is most abundant in the NW region that is directly exposed to westerlies (Fig. 3a). Among the northwestern mountain ranges, the highest climatological peak SWE values are found in the Pamir Mountains, Karakoram and the western Himalayas, with more than 1 m of peak SWE estimated. A significant amount of peak SWE is also estimated in the Tien Shan and Hindu Kush, showing peak SWE values of 1 m or less in the Tien Shan and 0.5 m or less in Hindu Kush in general (Fig. 3a). The estimates of peak SWE values in Hindu Kush are consistent with measurements and SWE reconstruction estimates from Salang Pass in Afghanistan (35° N, 69° E; elevation 3366 m) that has records of snow (Bair et al., 2018). The non-seasonal snow and ice are most notable in Karakoram but also evident in a few locations over the Pamir, Tien Shan and western Himalayas (Fig. 3b).

In contrast, seasonal snowpack is less abundant in the SE HMA (Fig. 3a), in part because it receives much of its precipitation in summer from the Indian and East Asia monsoons, while the winter westerlies have minimum impact. Shallow snowpack exists over the Hengduan Shan and Tanggula Shan, with low values of SWE estimated (less than 0.2 m). For the Himalayas and Nyainqêntanglha mountain ranges (Fig. 1), which exhibit extremely high elevation and receive significant summer precipitation from the monsoons, high values of SWE are estimated in some locations (Fig. 3b). However, those locations are largely masked out herein through the non-seasonal snow and ice mask (Fig. 3a), because the fSCA observations are persistently high throughout the year (no observed melt-out), show irregular temporal patterns without a clear accumulation–depletion cycle (non-seasonal) or are obscured by clouds between June–September (insufficient measurements), any of which can contribute to estimates of SWE that are less constrained due to cloud screening with potential errors of omission or commission in fSCA estimation.

The least abundant seasonal snowpack is estimated in the NE (Fig. 3a), where SWE is only notable over a few mountain ranges such as the Qilian Shan, Kunlun Shan and eastern Tibetan mountains. Despite their high elevations, most of the NE areas are snow-free or only have shallow and intermittent snow as a result of being further away from the primary atmospheric moisture sources.

Previous studies have also examined the spatiotemporal distribution in seasonal snowpack, regarding SCA (e.g., Pu et al., 2007; Basang et al., 2017), snow depth and SWE (e.g., Terzago et al., 2014; Bian et al., 2019; Orsolini et al., 2019), and the overall finding is that most existing datasets present consistent spatial patterns at large scales (e.g., regional) but differ greatly in the magnitudes of SWE and snow depth, which implies large uncertainties in snow mass estimates over this data-scarce region. Similarly, HMASR exhibits coherent spatial patterns compared to these previous efforts, yet the magnitudes of SWE still show significant variability. A more comprehensive analysis of HMA SWE between multiple products will be addressed in an upcoming intercomparison paper using HMASR.

### 3.1.2 Peak seasonal SWE timing

The timing of peak seasonal SWE occurrence is associated with climatological (e.g., precipitation) and topographic (e.g., elevation) factors and therefore shows significant heterogeneity over HMA. Figure 4 depicts the pixel-wise peak SWE day of water year (DOWY) climatology map. Highly

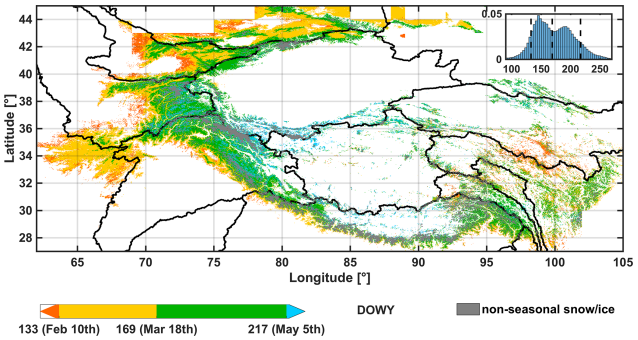


**Figure 4.** Map of pixel-wise peak seasonal SWE DOWY climatology, with non-seasonal snow and ice pixels masked out (gray). The inset figure is the histogram of peak SWE DOWY. The three dates labeled in the color bar (DOWY 133, DOWY 169 and DOWY 217) correspond to the 10th, 50th and 90th percentile in the DOWY distribution and are marked with vertical dashed lines in the inset histogram.

intermittent snow pixels were excluded, as well as permanent snow and ice pixels via the non-seasonal snow and ice mask. Peak SWE generally occurs between DOWY 100 and DOWY 250 for seasonal snow. Specifically, the date of peak SWE timing is characterized spatially by a median of DOWY 169 (18 March) and an interdecile range between DOWY 133 (10 February) and DOWY 217 (5 May), as shown in Fig. 4. However, the peak SWE DOWY shows a bimodal distribution (Fig. 4, inset), with the earlier peak centered on DOWY 145 and the later peak centered on DOWY 192.

For those mountain ranges in the NW, the northern and western mountain slopes of the Tien Shan, the western foothills of Pamir, the entire Hindu Kush, and the foothills of the western Himalayas all have relatively early peak SWE occurrences between 10 February and 18 March (Fig. 4). In contrast, the southern mountain slopes of the Tien Shan, the majority of the Pamir, Karakoram and western Himalaya show a relatively late peak SWE occurrence between 18 March and 5 May (Fig. 4). For those mountain ranges in the SE and NE, the peak SWE occurrence dates are more diverse (Fig. 4). In the SE, the central and eastern Himalayas, Nyainqêntanglha Mountains, and Hengduan Shan generally have later peak SWE occurrences (between 18 March and 5 May), except in the southern foothills, where peak SWE tends to occur earlier (between 10 February and 18 March). In the NE, the eastern Tibetan mountains show the earliest peak SWE occurrence dates (before 10 February), while the Qilian Shan and Kunlun Shan show the latest peak SWE occurrences (after 5 May).

#### 3.1.3 Seasonal SWE evolution

The spatial patterns of seasonal evolution of SWE, averaged over SON (September, October, November), DJF (December, January, February), MAM (March, April, May) and JJA (June, July, August), are shown in Fig. 5. As expected, higher SWE amounts are generally found in winter (DJF) and spring (MAM), while lower SWE amounts are found in summer (JJA) and fall (SON). Throughout the year, mountains in NW hold the maximum amount of SWE compared to other regions. In SON, the entire HMA region exhibits minimal SWE magnitudes (0.1 m or below) and most regions are snow-free (Fig. 5). During this period, SWE starts accumulating in the Tien Shan, Pamir and western Himalayas, which are directly facing the westerlies. SWE is also evident in the Nyainqêntanglha Mountains and Hengduan Shan, which are associated with the summer monsoons. In DJF, both the overall magnitude and extent of SWE grow significantly, with mean SWE values up to 0.5 m found in the Tien Shan, Pamir and western Himalayas (Fig. 5). The magnitude of SWE grows even larger in MAM, with up to 1 m SWE values estimated in the western HMA mountains and up to 0.5 m SWE values estimated in Nyainqêntanglha Mountains and the eastern Himalayas. Meanwhile, the extent of SWE shrinks significantly during MAM in the Hindu Kush and Tien Shan due to the weakened westerlies in spring. In JJA, both the magnitude and extent of SWE drop dramatically over most of the domain, with some exceptions of more persistent snowpack (with up to 0.3 m SWE) still evident in the Pamir, Karakoram and Nyainqêntanglha Mountains, where snow melts out slower than the surrounding regions.

### 3.2 Temporal distribution of seasonal SWE

Despite the significant literature on seasonal snowpack in this region, quantification of the regional-scale SWE volume is more difficult to obtain, partly due to the large uncertainties in SWE estimation over this region. In this section, the temporal variations in integrated seasonal SWE volumes across the major river basins are quantified, with the climatology presented in Sect. 3.2.1 and the interannual variations illustrated in Sect. 3.2.2.

#### 3.2.1 Climatology of seasonal SWE

The climatology of the seasonal cycle in SWE volumes that are integrated across HMA and its major river basins are quantified and presented in Fig. 6, with the key statistics of annual peak SWE volumes (peak of the annual time series) summarized for the entire HMA region and each basin in Table 1. Note again that the non-seasonal snow and ice mask has been applied when calculating the aggregated SWE volumes.

The HMA-wide SWE volume is presented in Fig. 6a, and the 18-year average of annual peak SWE volume is found to be 162.57 $km^3$ (note this is higher than the peak value in Fig. 6a, as it is the direct average of 18-year maxima rather than averaged across DOWY). The climatological peak SWE volume was further assessed in each subregion

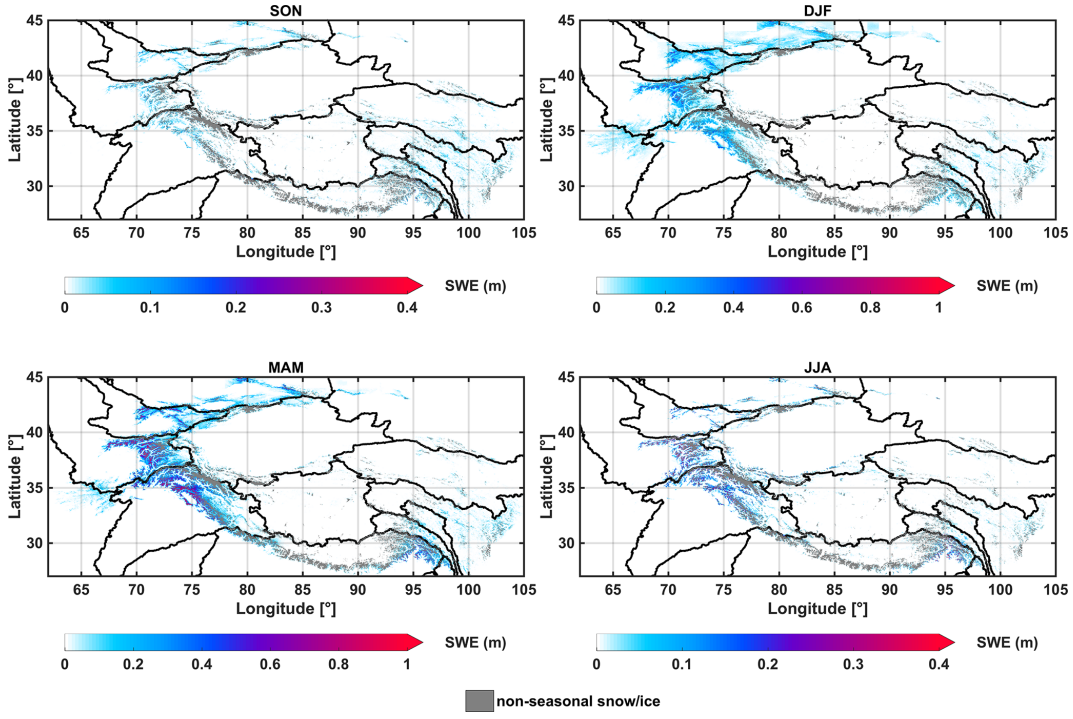


**Figure 5.** Map of mean seasonal SWE climatology in SON (September, October, November), DJF (December, January, February), MAM (March, April, May) and JJA (June, July, August), with non-seasonal snow and ice pixels masked out (gray).

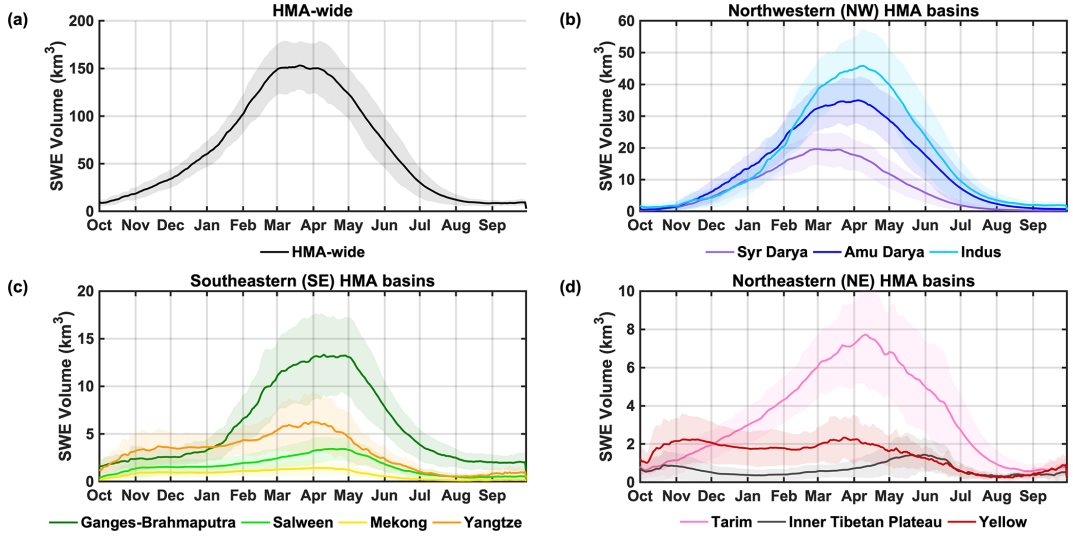


**Figure 6.** Climatological (18-year average; solid line) daily time series of seasonal SWE volumes, aggregated to **(a)** HMA-wide and basins in the **(b)** northwestern (NW), **(c)** southeastern (SE), and **(d)** northeastern (NE) subregions. The shaded area represents ±1 SD (standard deviation) around the climatological mean (i.e., representing a metric of interannual variation about the mean).

(i.e., within NW, NE and SE) and compared against that over the entire HMA (Table 1). The results show the highest peak SWE volume occurs in NW basins (107.42 $km^3$, ∼ 66 % of domain-wide total), followed by SE basins (29.49 $km^3$, ∼ 18 %) and NE basins (14.78 $km^3$, ∼ 9 %), which is coherent with the spatial pattern shown in Fig. 3a. Note that around ∼ 7 % of HMA-wide SWE volume falls in the regions outside of the watersheds examined (mainly in the northmost regions shown in Fig. 1), which is why these basin-scale quantities do not sum up to 100 % of the HMA-wide totals.

For the NW basins, the maximum amount of SWE volume is found in the Indus basin, followed by Amu Darya and Syr

**Table 1.** Summary statistics for HMA-wide and basin-scale annual peak SWE volume (peak of annual time series) assessed from the 18-year HMASR. The HMA-wide values are shown in the bold text. The subregional peak SWE volumes and their fractions relative to HMA-wide peak SWE volume are shown in the bold text as well.

| Region | Basin name | Peak SWE volume (peak of annual time series) | | | | | | | |
|---|---|---|---|---|---|---|---|---|---|
| | | Climatology | | | Interannual variability | | | | |
| | | Mean ($km^3$) | Total of subregional mean ($km^3$) | Standard deviation ($km^3$) | Coefficient of variation | Max ($km^3$) | Min ($km^3$) | Max year | Min year |
| HMA-wide | HMA-wide | **162.57** | **162.57 (100 %)** | **26.53** | **0.16** | **227.12** | **114.10** | **2005** | **2001** |
| Northwestern (NW) basins | Syr Darya | 21.16 | **107.42 (66 %)** | 5.19 | 0.25 | 29.88 | 13.61 | 2010 | 2000 |
| | Amu Darya | 37.31 | | 7.10 | 0.19 | 48.31 | 25.92 | 2017 | 2008 |
| | Indus | 48.95 | | 10.27 | 0.21 | 63.97 | 23.71 | 2009 | 2001 |
| Southeastern (SE) basins | Ganges–Brahmaputra | 15.59 | **29.49 (18 %)** | 3.84 | 0.25 | 25.40 | 10.69 | 2005 | 2009 |
| | Salween | 3.97 | | 1.23 | 0.31 | 6.71 | 2.21 | 2005 | 2002 |
| | Mekong | 1.92 | | 0.77 | 0.40 | 3.56 | 1.02 | 2000 | 2004 |
| | Yangtze | 8.02 | | 2.97 | 0.37 | 14.79 | 3.32 | 2005 | 2015 |
| Northeastern (NE) basins | Tarim | 8.78 | **14.78 (9 %)** | 2.45 | 0.28 | 12.92 | 4.81 | 2017 | 2007 |
| | Inner Tibetan Plateau | 2.35 | | 0.99 | 0.42 | 4.98 | 0.57 | 2013 | 2004 |
| | Yellow | 3.65 | | 1.25 | 0.34 | 6.10 | 1.76 | 2005 | 2004 |

Darya (Fig. 6b). The seasonality of basin-scale SWE in NW displays similar features to the HMA-wide SWE, with snow accumulating from October to March/April and depleting until the end of the WY. Meanwhile, the peak SWE volume is found to occur earlier and disappear faster in the Syr Darya basin, followed by Amu Darya and Indus. This is potentially attributed to their geographic locations, where Syr Darya is located further north and only affected by the winter westerlies; Indus is located further south and is partially affected by the summer monsoons.

For the SE basins, higher SWE volumes are found in Ganges–Brahmaputra, followed by Yangtze, Salween and Mekong (Fig. 6c). It is worthwhile to note that Ganges–Brahmaputra has an average peak SWE volume of 15.59 $km^3$, with an average carryover SWE volume of around 2 $km^3$ at the end of the WY (Fig. 6c). This amount of carryover SWE volume in Ganges–Brahmaputra is a result of the fact that (1) its mountain ranges (Himalayas) have higher elevation than those in other basins and (2) based on the non-seasonal snow and ice criterion (Sect. 2.4), a carryover SWE within 10 % of the maximum SWE in each year is allowed. Meanwhile, the seasonality in basin-scale SWE over SE is distinct across basins, e.g., the Ganges–Brahmaputra and Salween show more unimodal features (with obvious peaking in April–May), while the Yangtze and Mekong show more bimodal/uniform features, which are likely to be associated with the intermittent snowpack and summer monsoons.

For the NE basins over HMA, the overall magnitude of SWE volumes is smallest (Fig. 6d). These basins all have relatively large areas but are mostly snow-free or covered by shallow snow as depicted in Fig. 3a. Distinct seasonal features are also observed in these basins; e.g., a unimodal seasonal cycle of SWE is found in Tarim with an obvious peak in mid-April, while the Inner Tibetan Plateau and Yellow River basin show more uniform features that are potentially attributed to the intermittent snow, as they are further away from the moisture sources (limited influence by westerlies and monsoons).

### 3.2.2 Interannual variations in SWE and timing

In addition to the 18-year climatology of SWE volumes in Sect. 3.2.1, the interannual variations in HMA-wide and basin-scale peak SWE and its timing are further illustrated in Figs. 7–9 and Table 1. The aggregated seasonal SWE volume across HMA-wide or basin scales are visualized in the 18-year time series (Fig. 7), which illustrates a strong seasonal cycle and significant interannual variations in peak SWE. Over the record examined, the HMA-wide annual peak SWE volume (Table 1; Fig. 7) is found to be largest in WY 2005 with a value of 227.12 $km^3$, is found to be smallest in WY 2001 with a value of 114.10 $km^3$, and has a standard deviation of 26.53 $km^3$ (i.e., a coefficient of variation of 16 %). Basin-scale annual peak SWE volumes also exhibit significant variations, with their standard deviations ranging from 0.77 $km^3$ (coefficient of variation of 40 %) in the Mekong to 10.27 $km^3$ (coefficient of variation of 21 %) in the Indus. Moreover, different maximum/minimum years of peak SWE are found in each basin and are not always syn-

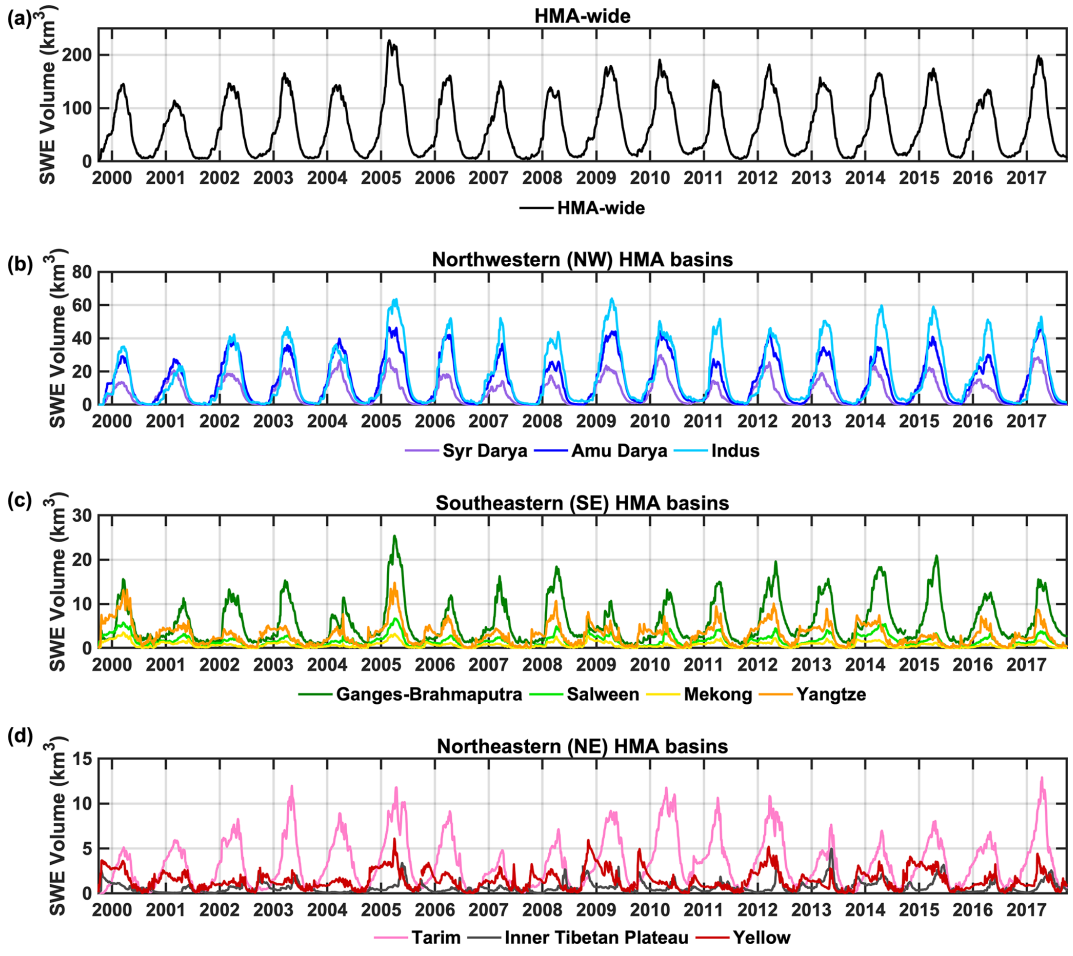


**Figure 7.** Daily time series of seasonal SWE volumes aggregated to **(a)** HMA-wide, **(b)** northwestern (NW), **(c)** southeastern (SE) and **(d)** northeastern (NE) basin totals.

chronous with the maximum/minimum years found in HMA-wide SWE (Table 1; Fig. 7).

When focusing on the HMA-wide seasonal cycle across different WYs (Fig. 8), it is found that snowpack quickly accumulates to over 10 $km^3$ in SWE volume during October, approaching $\sim 50\,\%$ of its peak SWE volume in January for most WYs and reaching a peak SWE volume within March and April, with an averaged timing of DOWY 168 (17 March) when averaged over 18 WYs. After peaking, the seasonal snowpack starts depleting and declines back to $\sim 50\,\%$ of its peak volume in May and June for most WYs. Snowpack depletes to under 10 $km^3$ in SWE volume between July and September, except in WYs 2009, 2010 and 2014, which have persistent snow across the entire year. The interannual variations across WYs are evident in (1) the variation in peak SWE volume and the peak dates, which range from 114 to 227 $km^3$ in volume and from late February (DOWY 146) to mid-April (DOWY 195); (2) the variation in the temporal window where the snow storage is more than 50 % of the peak SWE, which spans between 3.5 months (WY 2003) and 5.5 months (WY 2016); and (3) the variation in timing when snowpack depletes to under 10 $km^3$ in SWE volume, which ranges between July and October.

The basin-scale results (Fig. 9) show more variation compared to the HMA-wide results, with divergent peak SWE dates across basins and across WYs. The seasonal cycle observed in the NW and many other basins (Syr Darya, Amu Darya, Indus, Ganges–Brahmaputra and Tarim) is clearly influenced by winter westerlies, with SWE typically peaking around April and depleting in July–October, and that seasonality is consistent when examined across different WYs. The interannual variations in these basins are mainly reflected by (1) the overall magnitude of SWE volumes and (2) timing of snowpack occurrences/disappearances, while the peak SWE dates are closely centered around the climatological mean dates ($\sim$ April). However, different seasonal cycles are observed in the other basins (Mekong, Yangtze, Inner Tibetan Plateau and Yellow) that are more influenced by the summer monsoons, when examined across different WYs. For exam-

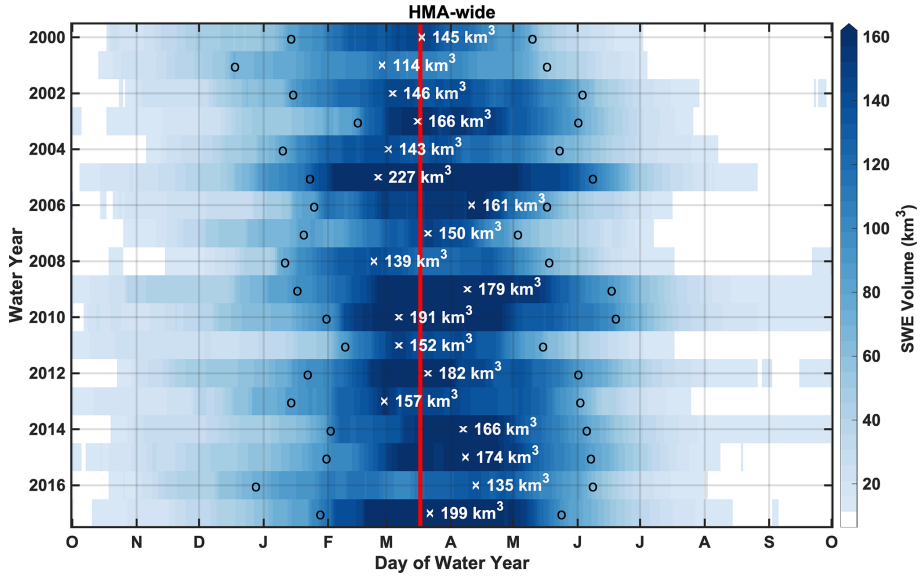


**Figure 8.** Daily time series of HMA-wide SWE volumes displayed as functions of DOWY and WY. The symbol "x" is used to mark the date of peak SWE volume occurrence, with the corresponding peak SWE volume labeled in each WY. The symbol "o" is used to mark the dates when 50 % of the peak SWE volume is reached in each WY. The vertical red line is used to indicate the 18-year average timing of HMA-wide peak SWE volume.

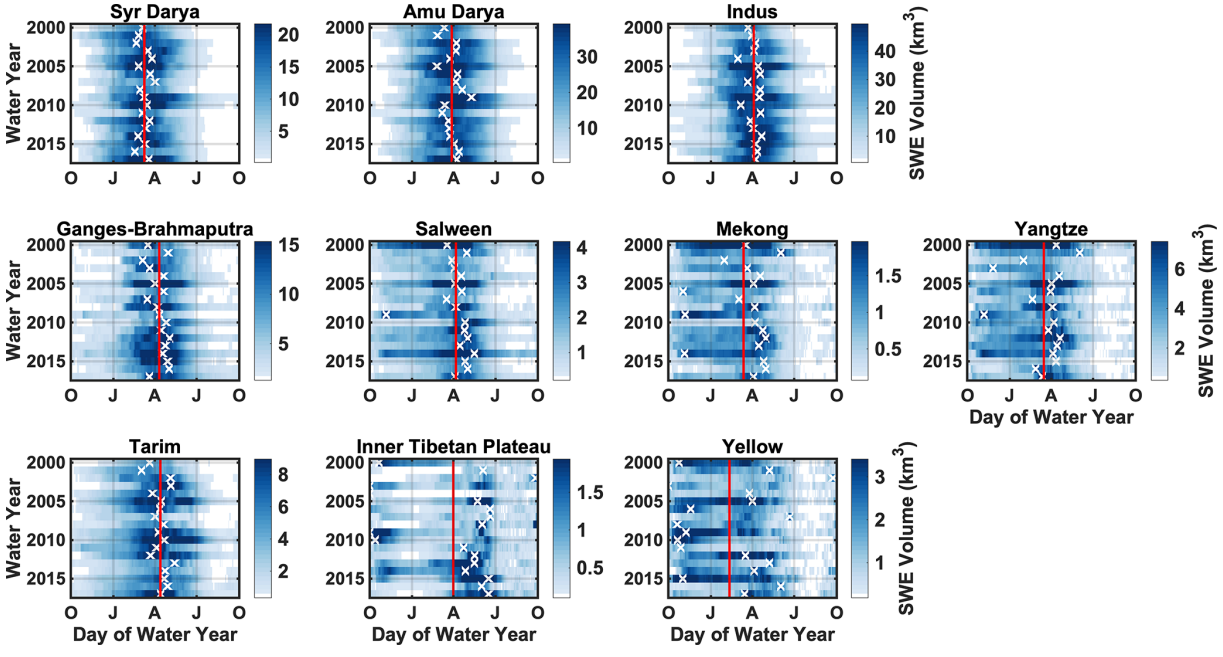


**Figure 9.** Daily time series of basin-scale SWE volumes displayed as functions of DOWY and WY. The symbol "x" is used to mark the date of basin-scale peak SWE volume occurrence in each WY. The vertical red line is used to indicate the 18-year average timing of basin-scale peak SWE volume.

ple, peak SWE may occur as early as October and as late as July within the same basin. The persistence of snow also varies across basins and WYs, with SWE being either persistently high across several months or intermittent over a short period of time. These factors explain the bimodal or uniform features in the SWE time series and its climatology (Figs. 6 and 7).

It is also worthwhile to note that the average peak SWE dates are in March and April for most basins, while it is not necessarily representative for some basins (e.g., Inner

Tibetan Plateau and Yellow) that have highly varying dates across years. Moreover, the average dates in many basins appear to be later than the HMA-wide average peak SWE date (17 March), mainly because a portion of the HMA-wide SWE falls in the northmost regions that is outside of the watersheds examined (above Syr Darya), and those regions are most influenced by the winter westerlies and reach peak SWE very early (before 19 March; Fig. 4).

### 3.3 Elevational distribution of seasonal SWE

The pixel-wise peak SWE distribution vs. elevation was assessed, both in terms of its 18-year averaged climatology (Sect. 3.3.1) and its variations under different climate conditions (Sect. 3.3.2). The HMA-wide domain and each basin were divided into 5-percentile elevation bins, so that the aggregated SWE volumes are calculated over comparable areas, following the method in Smith and Bookhagen (2018). The non-seasonal snow and ice pixels were removed when calculating peak seasonal SWE volume, and its fractional areal coverage within a given elevation band is computed to assess the relative elevational contributions to total seasonal SWE volume.

#### 3.3.1 Seasonal peak SWE climatology

When examining the SWE climatology over the full HMA domain (Fig. 10), the seasonal pixel-wise peak SWE volume was found to be largest at mid-elevations (3000–4000 m), with peak SWE values occurring at elevations around 3500 m (Fig. 10a and b, top row). The large increase in SWE from lower to mid-elevations is indicative of orographic enhancement, where the decrease at higher elevations is indicative of moisture limitations on orographic effects and/or increasing amounts of non-seasonal snow and ice. The presence of non-seasonal snow and ice becomes evident at elevations above 3500 m, and it increases dramatically above 5000 m, with a value up to 35 % (Fig. 10c, top row). When assessing the cumulative fraction of SWE volume as a function of elevation, it was found that over 50 % of HMA-wide seasonal SWE volume is stored at elevations above 3500 m, and less than 10 % of seasonal SWE volume is stored at elevations below 2000 m (Fig. 10d, top row).

The subregional elevational distribution of pixel-wise peak SWE climatology and its volume vary in each basin, compared to the HMA-wide results (Fig. 10). Relatively similar characteristics are observed in the NW basins (Syr Darya, Amu Darya and Indus), Tarim in the NE, and Ganges–Brahmaputra and Yangtze in the SE, where the pixel-wise peak SWE volumes (Fig. 10b) generally increase with elevation (below $\sim$ 4000 m) and then decline with elevation (above $\sim$ 4000 m), reaching their maximum values at mid-elevations (3000–4000 m). While the SWE distribution (Fig. 10a) is generally consistent with the SWE volume distribution (Fig. 10b) within these basins, the SWE values at high elevations (e.g., $\sim$ 6000 m) are large, contributing to a non-negligible amount of seasonal SWE volume at high elevations, despite the relatively high coverage of non-seasonal snow and ice (up to 60 %; Fig. 10c) above 4000 m in these basins. Moreover, for the cumulative fraction of SWE volumes above a specified elevation (Fig. 10d), unique median values are found within each basin, e.g., $\sim$ 4000 m (Indus, Ganges–Brahmaputra, Tarim), $\sim$ 3500 m (Amu Darya) or $\sim$ 2800 m (Syr Darya).

Other basins in SE (Salween, Mekong) and NE (Yellow, Inner Tibetan Plateau) generally show monotonically increasing SWE and SWE volumes against elevation (Fig. 10a and b). These basins feature relatively small SWE volumes and low coverage of non-seasonal snow and ice coverage (mostly under 25 %; Fig. 10c) at high elevations. For the cumulative fraction of SWE volumes above a specified elevation (Fig. 10d), the median values are found at higher elevations for SE and NE (between 4000–5200 m) basins.

#### 3.3.2 Variations under different climate conditions

The elevational distribution of peak SWE was also examined under different climate conditions (e.g., warm vs. cool years, wet vs. dry years) relative to normal conditions. Such analysis identifies whether different climate conditions affect the overall snow storage distribution across different elevations. For categorizing the different climate conditions, the HMA-wide winter precipitation and (near-surface) air temperature were used (Table 2), where winter (DJF) denotes the period from 1 December to 1 March. A "*k*-means" clustering analysis method (Lloyd, 1982) was used to seek classification of different climate conditions, based on the normalized winter precipitation and air temperature (subtracting the mean values and dividing by the standard deviations). The number of clusters to be classified is an input to the method; five clusters were specified in an attempt to group annual realizations into "normal", "wet", "dry", "warm" and "cool" categories. The classified clusters are displayed in Fig. 11, where the five clusters are logically grouped and interpreted as the categories mentioned above. It should be noted that there is a slight correlation (correlation coefficient of 0.29 with a $p$ value of 0.25) between annual realizations of precipitation and air temperature, indicating warmer years tend to be wetter years (but statistically insignificant due to the limited number of years).

Based on these clusters, the average pixel-wise peak SWE volumes under the same climate conditions are computed. The cluster-averaged peak SWE volumes under dry, normal and wet years are 209.6, 260.5 and 355.6 $km^3$, respectively. As shown in Fig. 12a, as expected, in spanning from dry to wet years there are marked increases in peak SWE volume over all elevations, particularly over the mid-elevations to low elevations (e.g., below 4000 m). In drier years, while Fig. 12a shows smaller SWE volumes across all elevations, the fractional SWE volumes are not always smallest, as

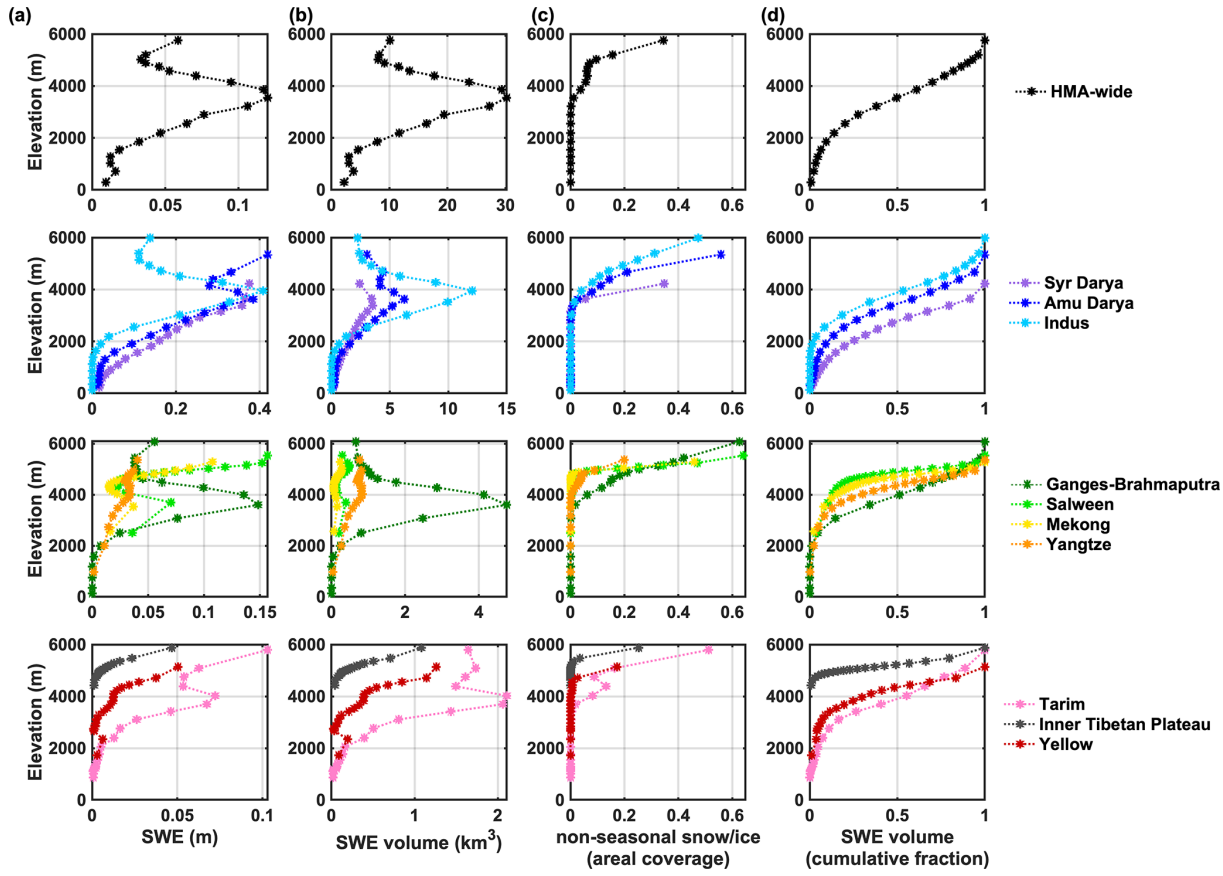


**Figure 10.** Pixel-wise peak seasonal **(a)** SWE climatology, **(b)** SWE volume climatology, **(c)** fractional areal coverage of non-seasonal snow and ice within each elevation band, and **(d)** cumulative fraction of SWE volume above the specified elevation, within HMA, northwestern (NW), southeastern (SE) and northeastern (NE) basins. Elevation is discretized into 5-percentile bins.

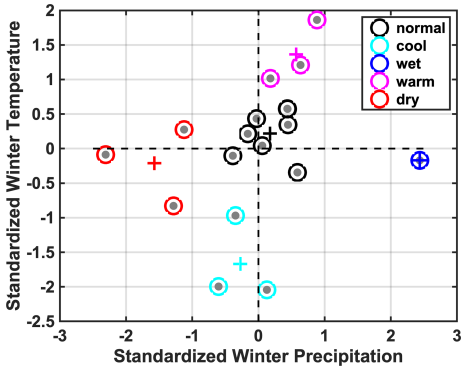


**Figure 11.** Category of different climate conditions from clustering analysis, based on the normalized winter precipitation and winter air temperature. Five clusters were identified as normal, wet, dry warm and cool conditions, with the centroid of each cluster marked with the "+" symbol.

shown in Fig. 12b. It can be observed that the fractional SWE volumes in dry years are smaller than those in normal years, in the low elevations to mid-elevations (∼ 1500–3600 m). At mid-to-high elevations (∼ 3600–5500 m), the dry years show greater fractional SWE volumes, compared to normal years. On the contrary, wet years show larger fractional SWE volumes below ∼ 3000 m and smaller fractional SWE volumes above ∼ 3000 m, when compared to normal years. Such differences in the fractional SWE volumes may be due to two potential factors: (1) the dry conditions generally have less humid air, which may have accelerated evaporation and snow sublimation at lower elevations prior to peak timing; and (2) a slight shift in snowfall/precipitation towards higher elevations during drier years due to orographic effects – i.e., precipitation tends to occur at higher elevations where the moist and less humid air is cold enough to reach condensation. Note that the cluster-averaged air temperature is quite consistent under wet/dry/normal conditions, which should minimize the effect of air temperature differences on snow distribution in Fig. 12a and b.

Similarly, the pixel-wise peak SWE distribution under warm, normal, and cool years are examined. The cluster-averaged peak SWE volumes under warm, normal and cool years are 285.34, 260.47 and 256.91 km$^3$, respectively, with cluster-averaged air temperatures of 263.30, 262.44 and

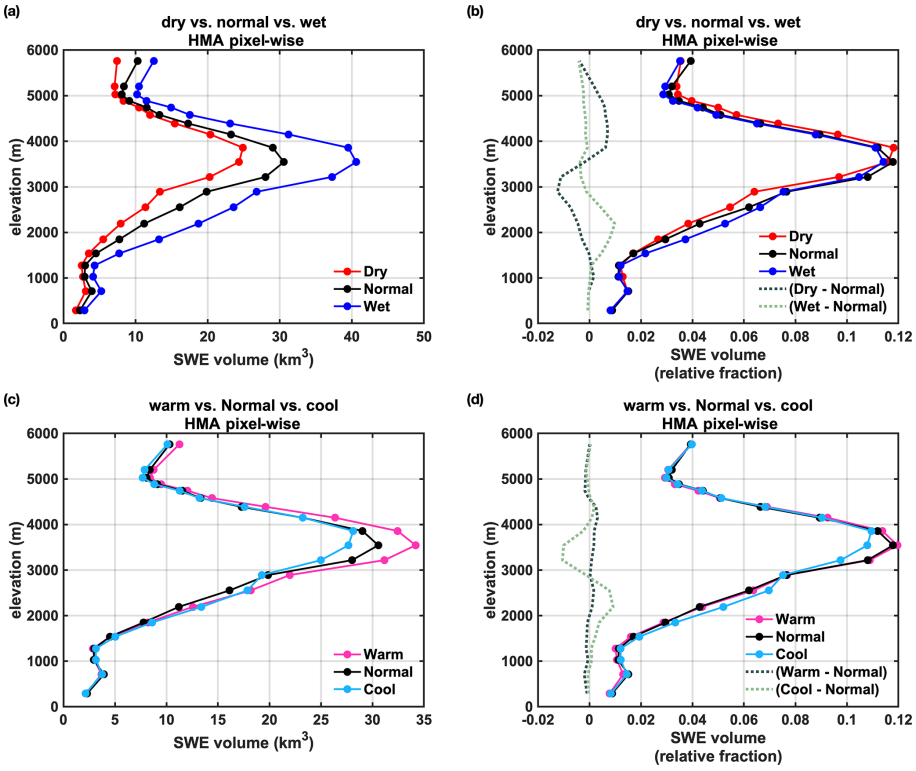


**Figure 12.** Cluster-averaged pixel-wise peak SWE volume (and its relative fraction, i.e., normalized with total SWE volume) distribution vs. elevation under different climate conditions in HMA. Here panels **(a)** and **(b)** show the distribution under dry, normal and wet conditions; panels **(c)** and **(d)** show the distribution under warm, normal and cool conditions. Difference curves with reference to the normal condition are also provided in panels **(b)** and **(d)** as shown with dashed lines.

261.01 K. It should be noted that the warm year cluster has greater peak SWE volumes (by $\sim 25\,km^3$) than the normal and cool years, which is reflected by the slightly higher precipitation in the warm year cluster (Fig. 11). Therefore, we put more emphasis on the fractional peak SWE distribution (Fig. 12d) here to eliminate the effect of overall snow volume on snow distribution. The results indicate that warm and normal years have very consistent distributions, when the fractional SWE volumes are examined (Fig. 12d). It is most notable that cool years have higher fractions of snow stored at lower elevations (e.g., below 3000 m) and smaller fractions of snow stored at mid-elevations (3000–4000 m) compared to normal and warm years (Fig. 12d, dotted lines). As the difference in air temperature between normal and cool years is $\sim 1.5$ K, this may indicate that the low-elevation snow storage tends to shift towards higher elevations (e.g., to mid-elevations) with 1.5 K of warming (from cool to normal conditions), when the overall snow storage is the same.

## 4 Conclusions

A first-order spatiotemporal analysis of seasonal SWE over the HMA region is presented in this paper, using a new 18-year snow reanalysis dataset (HMASR; Liu et al., 2021). This HMASR dataset is derived based on a previously developed snow reanalysis scheme (Margulis et al., 2019) that jointly assimilates fSCA observations from both Landsat and MODSCAG products, which has daily outputs of SWE and other snow variables, with a spatial resolution of 16 arcsec ($\sim 500$ m), over the joint period of Landsat and MODIS from WYs 2000 to 2017.

This work herein used the new HMASR dataset to address scientific questions aimed at characterizing how seasonal SWE and snow storage is distributed spatially, temporally and elevationally across and within HMA. In terms of the spatial distribution, seasonal snow is most abundant in the NW, with over 1 m of peak SWE observed over the mountain ranges. Seasonal snow is also significant in the SE, where both relatively deep snowpacks (with peak SWE values up to 1 m or above) and shallow snowpacks (with peak SWE up to 0.2 m) are found. Seasonal snow is less abundant in the NE where most areas are snow-free or only covered by shallow snowpacks (with peak SWE values below 0.2 m). The domain-wide median date of peak SWE is estimated to be 18 March with significant heterogeneity across this region, linked with climatological drivers and topography.

When aggregating the total SWE volumes across the full HMA domain and its basins, the climatological peak

**Table 2.** HMA pixel-wise peak SWE volume, winter precipitation volume and winter air temperature, with each year categorized as dry/normal/wet/warm/cool based on clustering classification.

| WY | Peak SWE | Winter | | Clustering |
|---|---|---|---|---|
| | volume pixel-wise ($km^3$) | Precipitation volume ($km^3$) | Air temperature (K) | category |
| 2000 | 214.08 | 251.51 | 261.65 | dry |
| 2001 | 187.97 | 204.28 | 262.21 | dry |
| 2002 | 240.66 | 309.23 | 262.60 | normal |
| 2003 | 266.22 | 330.72 | 262.71 | normal |
| 2004 | 235.36 | 313.29 | 262.31 | normal |
| 2005 | 355.55 | 422.90 | 262.14 | wet |
| 2006 | 254.80 | 318.94 | 263.04 | warm |
| 2007 | 224.51 | 303.16 | 262.43 | normal |
| 2008 | 249.79 | 316.56 | 260.73 | cool |
| 2009 | 294.83 | 339.96 | 263.19 | warm |
| 2010 | 313.81 | 331.18 | 262.53 | normal |
| 2011 | 237.69 | 294.65 | 261.54 | cool |
| 2012 | 283.24 | 282.77 | 260.77 | cool |
| 2013 | 263.14 | 337.68 | 262.01 | normal |
| 2014 | 273.41 | 292.81 | 262.19 | normal |
| 2015 | 266.62 | 330.90 | 262.71 | normal |
| 2016 | 226.62 | 258.84 | 262.48 | dry |
| 2017 | 306.40 | 351.42 | 263.68 | warm |

seasonal SWE volume was found to be 163 $km^3$, with NW basins accounting for around 66 % of that volume, followed by SE ($\sim$ 18 %) and NE ($\sim$ 9 %) basins. The seasonal cycle of HMA-wide SWE is depicted by snow accumulating through October to March and April, typically peaking around April and depleting in July–October. When examined at basin scales, similar seasonality is observed in the westerly-affected basins (e.g., in NW), while different SWE seasonality is observed in monsoon-affected basins (in SE and NE). Interannual variations in HMA-wide or basin-scale SWE are also evident, with peak SWE volumes ranging from 114 to 227 $km^3$ and peak dates ranging from late February (DOWY 146) to mid-April (DOWY 195), when examined over the HMA scale. The basin-scale SWE is more different from the HMA-wide SWE, where peak SWE may occur as early as October and as late as July, and is divergent across basins and across WYs.

The climatology of HMA-wide seasonal peak SWE is found to be most abundant at mid-elevations (3000–4000 m), with over 50 % of the seasonal SWE volume stored at elevations above 3500 m. When comparing wet, normal and dry years, we found that years with above-average amounts of precipitation cause a significant overall increase in SWE volumes across all elevations. Meanwhile, a slight increase in air temperature (e.g., $\sim$ 1.5 K) from cooler to normal years mainly leads to a redistribution in snow storage from lower elevations to mid-elevations, when the overall snow volume is the same.

This HMASR dataset is presented to augment the spatiotemporal gaps in previous SWE datasets and provide better characterization of spatiotemporal patterns in seasonal snowpack over the HMA region, especially over the mountainous areas with complex terrain where existing products tend to underestimate SWE and present large uncertainties (Wrzesien et al., 2019; Kim et al., 2021). It should prove useful in providing more insight into the role of seasonal snowpack in the regional hydrological cycle, as a verification dataset for atmospheric and other models, and in other applications where a space–time continuous snow dataset constrained by remote-sensing data is needed.

It should be noted that the reanalysis method is generally expected to work best for seasonal snow where there is a strong signature between snow disappearance and measured fSCA. Hence an important caveat is that non-seasonal snow pixels are likely to be more erroneous than the seasonal snow pixels. The use of a non-seasonal vs. seasonal snow mask is used in this paper to highlight the part of snow storage that is deemed seasonal snow. In the raw dataset, all pixels are provided and so users are free to take advantage of the non-seasonal snow estimates (with the caveat mentioned above). For the purposes of highlighting a new estimate of seasonal snow climatology in this paper, we focus on seasonal snow alone.

It is also acknowledged that the reanalysis method is best designed for non-ephemeral snow where there is a strong seasonal cycle and signal between snow disappearance and measured fSCA that can be captured at the frequency of the fSCA measurements. Hence ephemeral snow (i.e., shallow and intermittent) may not be fully captured. Finally, the accuracy of fSCA retrievals is likely not as high in the monsoon-dominated parts of HMA, which in our case excludes many more Landsat/MODSCAG measurements, resulting in higher uncertainty in SWE estimation over affected subregions like the Himalayas. Other remote-sensing approaches (e.g., active microwave measurements) that could penetrate clouds may potentially aid in reducing the uncertainties for SWE estimation over those areas. More research can be done to address such issues and improve the accuracy of SWE estimates for those regions in the future.

*Data availability.* The HMASR dataset used in this paper is publicly available on National Snow and Ice Data Center (NSIDC) HiMAT data repository, entitled High Mountain Asia UCLA Daily Snow Reanalysis, Version 1. It can be accessed through https://nsidc.org/data/HMA_SR_D/ (last access: 22 April 2021) or https://doi.org/10.5067/HNAUGJQXSCVU (Liu et al., 2021). The dataset is provided as NetCDF files for each $1^\circ \times 1^\circ$ tile shown in Fig. 1, available at 16 arcsec ($\sim$ 500 m) and daily resolution from WYs 2000 to 2017. Posterior estimates of other key snowpack properties (i.e., in addition to SWE) not focused on herein (e.g., snow depth, fSCA, snowmelt, sublimation and snow albedo) along with posterior forcing variables are included in this dataset. Data quality information, containing a classification mask and the non-seasonal

snow/ice mask, can be found in the dataset as well. Future versions of the dataset could extend it to include other years, provide estimates at higher spatial resolutions, and better characterize uncertainties through inclusion of other meteorological forcings and other inputs to the reanalysis framework.

*Author contributions.* YL led the production of the dataset and led the analysis in the manuscript. YF contributed to the production of the dataset and contributed to the analysis in the manuscript. SM supervised the project and provided guidance. All authors contributed to writing the manuscript.

*Competing interests.* The contact author has declared that neither they nor their co-authors have any competing interests.

*Disclaimer.* Publisher's note: Copernicus Publications remains neutral with regard to jurisdictional claims in published maps and institutional affiliations.

*Acknowledgements.* We would like to thank those responsible for the creation of the datasets used in this study as well as members of the NASA High Mountain Asia Team (HiMAT) who helped shape the overall direction of the work. Gonzalo Cortés is acknowledged for pre-processing some of the input data used to develop the HMASR dataset.

*Financial support.* This research was funded by the NASA High Mountain Asia program (grant no. NNX16AQ63G) with additional support provided by the National Science Foundation (grant no. 1641960).

*Review statement.* This paper was edited by Chris Derksen and reviewed by Edward Bair and one anonymous referee.

## References

Ahmad, J. A., Forman, B. A., and Kwon, Y.: Analyzing Machine Learning Predictions of Passive Microwave Brightness Temperature Spectral Difference Over Snow-Covered Terrain in High Mountain Asia, Front. Earth Sci., 7, 249, https://doi.org/10.3389/feart.2019.00212, 2019.

Armstrong, R. L., Rittger, K., Brodzik, M. J., Racoviteanu, A., Barrett, A. P., Khalsa, S.-J. S., Raup, B., Hill, A. F., Khan, A. L., Wilson, A. M., Kayastha, R. B., Fetterer, F., and Armstrong, B.: Runoff from glacier ice and seasonal snow in High Asia: separating melt water sources in river flow, Reg. Environ. Change, 19, 1249–1261, 2019.

Bair, E., Stillinger, T., Rittger, K., and Skiles, M.: COVID-19 lockdowns show reduced pollution on snow and ice in the Indus River Basin, P. Natl. Acad. Sci. USA, 118, e2101174118, https://doi.org/10.1073/pnas.2101174118, 2021.

Bair, E. H., Abreu Calfa, A., Rittger, K., and Dozier, J.: Using machine learning for real-time estimates of snow water equivalent in the watersheds of Afghanistan, The Cryosphere, 12, 1579–1594, https://doi.org/10.5194/tc-12-1579-2018, 2018.

Bair, E. H., Rittger, K., Ahmad, J. A., and Chabot, D.: Comparison of modeled snow properties in Afghanistan, Pakistan, and Tajikistan, The Cryosphere, 14, 331–347, https://doi.org/10.5194/tc-14-331-2020, 2020.

Barnett, T. P., Adam, J. C., and Lettenmaier, D. P.: Potential impacts of a warming climate on water availability in snow-dominated regions, Nature, 438, 303–309, 2005.

Basang, D., Barthel, K., and Olseth, J. A.: Satellite and Ground Observations of Snow Cover in Tibet during 2001–2015, Remote Sens., 9, 1201, https://doi.org/10.3390/rs9111201, 2017.

Bian, Q., Xu, Z., Zhao, L., Zhang, Y.-F., Zheng, H., Shi, C., Zhang, S., Xie, C., and Yang, Z.-L.: Evaluation and Intercomparison of Multiple Snow Water Equivalent Products over the Tibetan Plateau, J. Hydrometeorol., 20, 2043–2055, https://doi.org/10.1175/JHM-D-19-0011.1, 2019.

Bolch, T., Kulkarni, A., Kääb, A., Huggel, C., Paul, F., Cogley, J. G., Frey, H., Kargel, J. S., Fujita, K., Scheel, M., Bajracharya, S., and Stoffel, M.: The state and fate of Himalayan glaciers, Science, 336, 310–314, https://doi.org/10.1126/science.1215828, 2012.

Bolch, T., Shea, J. M., Liu, S., Azam, F. M., Gao, Y., Gruber, S., Immerzeel, W. W., Kulkarni, A., Li, H., Tahir, A. A., Zhang, G., and Zhang, Y.: Status and Change of the Cryosphere in the Extended Hindu Kush Himalaya Region, in: The Hindu Kush Himalaya Assessment: Mountains, Climate Change, Sustainability and People, edited by: Wester, P., Mishra, A., Mukherji, A., and Shrestha, A. B., Springer International Publishing, Cham, 209–255, 2019.

Bookhagen, B. and Burbank, D. W.: Toward a complete Himalayan hydrological budget: Spatiotemporal distribution of snowmelt and rainfall and their impact on river discharge, J. Geophys. Res., 115, 39, https://doi.org/10.1029/2009JF001426, 2010.

Bormann, K. J., Brown, R. D., Derksen, C., and Painter, T. H.: Estimating snow-cover trends from space, Nat. Clim. Change, 8, 924–928, 2018.

Chang, A. T. C., Foster, J. L., and Hall, D. K.: Nimbus-7 SMMR Derived Global Snow Cover Parameters, Ann. Glaciol., 9, 39–44, 1987.

Che, T., Li, X., Jin, R., Armstrong, R., and Zhang, T.: Snow depth derived from passive microwave remote-sensing data in China, Ann. Glaciol., 49, 145–154, 2008.

Cortés, G. and Margulis, S.: Impacts of El Niño and La Niña on interannual snow accumulation in the Andes: Results from a high-resolution 31 year reanalysis, Geophys. Res. Lett., 44, 6859–6867, https://doi.org/10.1002/2017GL073826, 2017.

Cortés, G., Girotto, M., and Margulis, S. A.: Analysis of sub-pixel snow and ice extent over the extratropical Andes using spectral unmixing of historical Landsat imagery, Remote Sens. Environ., 141, 64–78, 2014.

Dahe, Q., Shiyin, L., and Peiji, L.: Snow Cover Distribution, Variability, and Response to Climate Change in Western China, J. Climate, 19, 1820–1833, https://doi.org/10.1175/JCLI3694.1, 2006.

Dai, L., Che, T., Ding, Y., and Hao, X.: Evaluation of snow cover and snow depth on the Qinghai–Tibetan Plateau derived from

passive microwave remote sensing, The Cryosphere, 11, 1933–1948, https://doi.org/10.5194/tc-11-1933-2017, 2017.

Dee, D. P., Uppala, S. M., Simmons, A. J., Berrisford, P., Poli, P., Kobayashi, S., Andrae, U., Balmaseda, M. A., Balsamo, G., Bauer, P., Bechtold, P., Beljaars, A. C. M., van de Berg, L., Bidlot, J., Bormann, N., Delsol, C., Dragani, R., Fuentes, M., Geer, A. J., Haimberger, L., Healy, S. B., Hersbach, H., Hólm, E. V., Isaksen, L., Kållberg, P., Köhler, M., Matricardi, M., McNally, A. P., Monge-Sanz, B. M., Morcrette, J. J., Park, B. K., Peubey, C., de Rosnay, P., Tavolato, C., Thépaut, J. N., and Vitart, F.: The ERA-Interim reanalysis: configuration and performance of the data assimilation system, Q. J. Roy. Meteorol. Soc., 137, 553–597, https://doi.org/10.1002/qj.828, 2011.

Dozier, J.: Spectral signature of alpine snow cover from the landsat thematic mapper, Remote Sens. Environ., 28, 9–22, https://doi.org/10.1016/0034-4257(89)90101-6, 1989.

Dozier, J., Bair, E. H., and Davis, R. E.: Estimating the spatial distribution of snow water equivalent in the world's mountains, WIREs Water, 3, 461–474, https://doi.org/10.1002/wat2.1140, 2016.

Durand, M., Molotch, N. P., and Margulis, S. A.: A Bayesian approach to snow water equivalent reconstruction, J. Geophys. Res., 113, 872, https://doi.org/10.1029/2008JD009894, 2008.

Gelaro, R., McCarty, W., Suárez, M. J., Todling, R., Molod, A., Takacs, L., Randles, C. A., Darmenov, A., Bosilovich, M. G., Reichle, R., Wargan, K., Coy, L., Cullather, R., Draper, C., Akella, S., Buchard, V., Conaty, A., da Silva, A. M., Gu, W., Kim, G.-K., Koster, R., Lucchesi, R., Merkova, D., Nielsen, J. E., Partyka, G., Pawson, S., Putman, W., Rienecker, M., Schubert, S. D., Sienkiewicz, M., and Zhao, B.: The Modern-Era Retrospective Analysis for Research and Applications, Version 2 (MERRA-2), J. Climate, 30, 5419–5454, 2017.

Global Modeling and Assimilation Office (GMAO): MERRA-2 tavg1_2d_flx_Nx: 2d, 1-Hourly, Time-Averaged, Single-Level, Assimilation, Surface Flux Diagnostics V5.12.4, Greenbelt, MD, USA, Goddard Earth Sciences Data and Information Services Center (GES DISC) [dataset], https://doi.org/10.5067/7MCPBJ41Y0K6, 2015a.

Global Modeling and Assimilation Office (GMAO): MERRA-2 tavg1_2d_rad_Nx: 2d, 1-Hourly, Time-Averaged, Single-Level, Assimilation, Radiation Diagnostics V5.12.4, Greenbelt, MD, USA, Goddard Earth Sciences Data and Information Services Center (GES DISC) [dataset], https://doi.org/10.5067/Q9QMY5PBNV1T, 2015b.

Global Modeling and Assimilation Office (GMAO): MERRA-2 tavg1_2d_slv_Nx: 2d, 1-Hourly, Time-Averaged, Single-Level, Assimilation, Single-Level Diagnostics V5.12.4, Greenbelt, MD, USA, Goddard Earth Sciences Data and Information Services Center (GES DISC) [dataset], https://doi.org/10.5067/VJAFPLI1CSIV, 2015c.

Girotto, M., Margulis, S. A., and Durand, M.: Probabilistic SWE reanalysis as a generalization of deterministic SWE reconstruction techniques, Hydrol. Process., 28, 3875–3895, https://doi.org/10.1002/hyp.9887, 2014.

Hall, D. K., Riggs, G. A., Salomonson, V. V., DiGirolamo, N. E., and Bayr, K. J.: MODIS snow-cover products, Remote Sens. Environ., 83, 181–194, 2002.

Hansen, M. C., Defries, R. S., Townshend, J. R. G., and Sohlberg, R.: Global land cover classification at 1 km spatial resolution using a classification tree approach, Int. J. Remote Sens., 21, 1331–1364, https://doi.org/10.1080/014311600210209 2000.

Hersbach, H., Bell, B., Berrisford, P., Hirahara, S., Horányi, A., Muñoz Sabater, J., Nicolas, J., Peubey, C., Radu, R., Schepers, D., Simmons, A., Soci, C., Abdalla, S., Abellan, X., Balsamo, G., Bechtold, P., Biavati, G., Bidlot, J., Bonavita, M., Chiara, G., Dahlgren, P., Dee, D., Diamantakis, M., Dragani, R., Flemming, J., Forbes, R., Fuentes, M., Geer, A., Haimberger, L., Healy, S., Hogan, R. J., Hólm, E., Janisková, M., Keeley, S., Laloyaux, P., Lopez, P., Lupu, C., Radnoti, G., Rosnay, P., Rozum, I., Vamborg, F., Villaume, S., and Thépaut, J. N.: The ERA5 global reanalysis, Q. J. Roy. Meteorol. Soc., 146, 1999–2049, https://doi.org/10.1002/qj.3803, 2020.

Immerzeel, W. W. and Bierkens, M. F. P.: Asia's water balance, Nat. Geosci., 5, 841–842, 2012.

Immerzeel, W. W., Droogers, P., de Jong, S. M., and Bierkens, M. F. P.: Large-scale monitoring of snow cover and runoff simulation in Himalayan river basins using remote sensing, Remote Sens. Environ., 113, 40–49, 2009.

Immerzeel, W. W., van Beek, L. P. H., and Bierkens, M. F. P.: Climate Change Will Affect the Asian Water Towers, Science, 328, 1382, https://doi.org/10.1126/science.1183188, 2010.

Immerzeel, W. W., Lutz, A. F., Andrade, M., Bahl, A., Biemans, H., Bolch, T., Hyde, S., Brumby, S., Davies, B. J., Elmore, A. C., Emmer, A., Feng, M., Fernández, A., Haritashya, U., Kargel, J. S., Koppes, M., Kraaijenbrink, P. D. A., Kulkarni, A. V., Mayewski, P. A., Nepal, S., Pacheco, P., Painter, T. H., Pellicciotti, F., Rajaram, H., Rupper, S., Sinisalo, A., Shrestha, A. B., Viviroli, D., Wada, Y., Xiao, C., Yao, T., and Baillie, J. E. M.: Importance and vulnerability of the world's water towers, Nature, 577, 364–369, 2020.

Kääb, A., Berthier, E., Nuth, C., Gardelle, J., and Arnaud, Y.: Contrasting patterns of early twenty-first-century glacier mass change in the Himalayas, Nature, 488, 495–498, 2012.

Kim, R. S., Kumar, S., Vuyovich, C., Houser, P., Lundquist, J., Mudryk, L., Durand, M., Barros, A., Kim, E. J., Forman, B. A., Gutmann, E. D., Wrzesien, M. L., Garnaud, C., Sandells, M., Marshall, H. P., Cristea, N., Pflug, J. M., Johnston, J., Cao, Y., Mocko, D., and Wang, S.: Snow Ensemble Uncertainty Project (SEUP): quantification of snow water equivalent uncertainty across North America via ensemble land surface modeling, The Cryosphere, 15, 771–791, https://doi.org/10.5194/tc-15-771-2021, 2021.

Kirkham, J. D., Koch, I., Saloranta, T. M., Litt, M., Stigter, E. E., Møen, K., Thapa, A., Melvold, K., and Immerzeel, W. W.: Near Real-Time Measurement of Snow Water Equivalent in the Nepal Himalayas, Front. Earth Sci., 7, 677, https://doi.org/10.3389/feart.2019.00177, 2019.

Kobayashi, S., Oto, Y., Harada, Y., Ebita, A., Moriya, M., Onoda, H., Onogi, K., Kamahori, H., Kobayashi, C., Endo, H., Miyaoka, K., and Takahashi, K.: The JRA-55 Reanalysis: General Specifications and Basic Characteristics TI, J. Meteorol. Soc. Jpn. Ser. II, 93, 5–48, 2015.

Largeron, C., Dumont, M., Morin, S., Boone, A., Lafaysse, M., Metref, S., Cosme, E., Jonas, T., Winstral, A., and Margulis, S. A.: Toward Snow Cover Estimation in Mountainous Areas Using Modern Data Assimilation Methods: A Review, Front. Earth Sci., 8, 325, https://doi.org/10.3389/feart.2020.00325, 2020.

Lehner, B., Verdin, K., and Jarvis, A.: New Global Hydrography Derived From Spaceborne Elevation Data, Eos Trans. AGU, 89, 93–94, https://doi.org/10.1029/2008EO100001, 2008.

Lettenmaier, D. P., Alsdorf, D., Dozier, J., Huffman, G. J., Pan, M., and Wood, E. F.: Inroads of remote sensing into hydrologic science during the WRR era, Water Resour. Res., 51, 7309–7342, https://doi.org/10.1002/2015WR017616, 2015.

Lievens, H., Demuzere, M., Marshall, H.-P., Reichle, R. H., Brucker, L., Brangers, I., de Rosnay, P., Dumont, M., Girotto, M., Immerzeel, W. W., Jonas, T., Kim, E. J., Koch, I., Marty, C., Saloranta, T., Schöber, J., and De Lannoy, G. J. M.: Snow depth variability in the Northern Hemisphere mountains observed from space, Nat. Commun., 10, 4629, https://doi.org/10.1038/s41467-019-12566-y, 2019.

Liston, G. E.: Representing Subgrid Snow Cover Heterogeneities in Regional and Global Models, J. Climate, 17, 1381–1397, 2004.

Liu, Y. and Margulis, S. A.: Deriving Bias and Uncertainty in MERRA-2 Snowfall Precipitation Over High Mountain Asia, Front. Earth Sci., 7, 39, https://doi.org/10.3389/feart.2019.00280, 2019.

Liu, Y., Fang, Y., and Margulis, S. A.: High Mountain Asia UCLA Daily Snow Reanalysis, Version 1, NASA Snow and Ice Data Center Distributed Active Archive Center [data set], Boulder, Colorado, USA, https://doi.org/10.5067/HNAUGJQXSCVU, 2021.

Lloyd, S.: Least squares quantization in PCM, IEEE T. Inform. Theor., 28, 129–137, 1982.

Lutz, A. F., Immerzeel, W. W., Shrestha, A. B., and Bierkens, M. F. P.: Consistent increase in High Asia's runoff due to increasing glacier melt and precipitation, Nat. Clim. Change, 4, 587–592, 2014.

Margulis, S. A., Girotto, M., Cortés, G., and Durand, M.: A Particle Batch Smoother Approach to Snow Water Equivalent Estimation, J. Hydrometeorol., 16, 1752–1772, 2015.

Margulis, S. A., Cortés, G., Girotto, M., and Durand, M.: A Landsat-Era Sierra Nevada Snow Reanalysis (1985–2015), J. Hydrometeorol., 17, 1203–1221, 2016.

Margulis, S. A., Liu, Y., and Baldo, E.: A Joint Landsat- and MODIS-Based Reanalysis Approach for Midlatitude Montane Seasonal Snow Characterization, Front. Earth Sci., 7, 4257, https://doi.org/10.3389/feart.2019.00272, 2019.

Maussion, F., Scherer, D., Finkelnburg, R., Richters, J., Yang, W., and Yao, T.: WRF simulation of a precipitation event over the Tibetan Plateau, China – an assessment using remote sensing and ground observations, Hydrol. Earth Syst. Sci., 15, 1795–1817, https://doi.org/10.5194/hess-15-1795-2011, 2011.

Maussion, F., Scherer, D., Mölg, T., Collier, E., Curio, J., and Finkelnburg, R.: Precipitation Seasonality and Variability over the Tibetan Plateau as Resolved by the High Asia Reanalysis, J. Climate, 27, 1910–1927, https://doi.org/10.1175/JCLI-D-13-00282.1, 2014.

Mortimer, C., Mudryk, L., Derksen, C., Luojus, K., Brown, R., Kelly, R., and Tedesco, M.: Evaluation of long-term Northern Hemisphere snow water equivalent products, The Cryosphere, 14, 1579–1594, https://doi.org/10.5194/tc-14-1579-2020, 2020.

Mudryk, L. R., Derksen, C., Kushner, P. J., and Brown, R.: Characterization of Northern Hemisphere Snow Water Equivalent Datasets, 1981–2010, J. Climate, 28, 8037–8051, https://doi.org/10.1175/JCLI-D-15-0229.1, 2015.

Notarnicola, C.: Observing Snow Cover and Water Resource Changes in the High Mountain Asia Region in Comparison with Global Mountain Trends over 2000–2018, Remote Sens., 12, 3913, https://doi.org/10.3390/rs12233913, 2020.

Orsolini, Y., Wegmann, M., Dutra, E., Liu, B., Balsamo, G., Yang, K., de Rosnay, P., Zhu, C., Wang, W., Senan, R., and Arduini, G.: Evaluation of snow depth and snow cover over the Tibetan Plateau in global reanalyses using in situ and satellite remote sensing observations, The Cryosphere, 13, 2221–2239, https://doi.org/10.5194/tc-13-2221-2019, 2019.

Osmanoglu, B., Painter, T. H., Shean, D., Arendt, A., Kargel, J., and Margulis, S. A.: Remote sensing of the cryosphere in high mountain ASIA, in: 2017 IEEE International Geoscience and Remote Sensing Symposium (IGARSS), 2813–2816, 23-28 July 2017, Fort Worth, TX, USA, https://doi.org/10.1109/IGARSS.2017.8127583, 2017.

Painter, T. H., Dozier, J., Roberts, D. A., Davis, R. E., and Green, R. O.: Retrieval of subpixel snow-covered area and grain size from imaging spectrometer data, Remote Sens. Environ., 85, 64–77, 2003.

Painter, T. H., Rittger, K., McKenzie, C., Slaughter, P., Davis, R. E., and Dozier, J.: Retrieval of subpixel snow covered area, grain size, and albedo from MODIS, Remote Sens. Environ., 113, 868–879, 2009.

Painter, T. H., Brodzik, M. J., Racoviteanu, A., and Armstrong, R.: Automated mapping of Earth's annual minimum exposed snow and ice with MODIS, Geophys. Res. Lett., 39, 2012GL053340, https://doi.org/10.1029/2012GL053340, 2012.

Palazzi, E., von Hardenberg, J., and Provenzale, A.: Precipitation in the Hindu-Kush Karakoram Himalaya: Observations and future scenarios, J. Geophys. Res.-Atmos., 118, 85–100, https://doi.org/10.1029/2012JD018697, 2013.

Pfeffer, W. T., Arendt, A. A., Bliss, A., Bolch, T., Cogley, J. G., Gardner, A. S., Hagen, J.-O., Hock, R., Kaser, G., Kienholz, C., Miles, E. S., Moholdt, G., Mölg, N., Paul, F., Radić, V., Rastner, P., Raup, B. H., Rich, J., and Sharp, M. J.: The Randolph Glacier Inventory: a globally complete inventory of glaciers, J. Glaciol., 60, 537–552, 2014.

Pu, Z., Xu, L., and Salomonson, V. V.: MODIS/Terra observed seasonal variations of snow cover over the Tibetan Plateau, Geophys. Res. Lett., 34, 32141, https://doi.org/10.1029/2007GL029262, 2007.

Pulliainen, J., Luojus, K., Derksen, C., Mudryk, L., Lemmetyinen, J., Salminen, M., Ikonen, J., Takala, M., Cohen, J., Smolander, T., and Norberg, J.: Patterns and trends of Northern Hemisphere snow mass from 1980 to 2018, Nature, 581, 294–298, 2020.

Raup, B., Racoviteanu, A., Khalsa, S.-J. S., Helm, C., Armstrong, R., and Arnaud, Y.: The GLIMS geospatial glacier database: A new tool for studying glacier change, Global Planet. Change, 56, 101–110, 2007.

RGI Consortium: Randolph Glacier Inventory – A Dataset of Global Glacier Outlines: Version 6.0: Technical Report, Global Land Ice Measurements from Space, Colorado, USA, Digital Media, https://doi.org/10.7265/N5-RGI-60, 2017

Rienecker, M. M., Suárez, M. J., Gelaro, R., Todling, R., Bacmeister, J., Liu, E., Bosilovich, M. G., Schubert, S. D., Takacs, L., Kim, G.-K., Bloom, S., Chen, J., Collins, D., Conaty, A., da Silva, A., Gu, W., Joiner, J., Koster, R. D., Lucchesi, R., Molod, A., Owens, T., Pawson, S., Pegion, P., Redder, C. R., Reichle,

R., Robertson, F. R., Ruddick, A. G., Sienkiewicz, M., and Woollen, J.: MERRA: NASA's Modern-Era Retrospective Analysis for Research and Applications, J. Climate, 24, 3624–3648, https://doi.org/10.1175/JCLI-D-11-00015.1, 2011.

Rodell, M., Houser, P. R., Jambor, U., Gottschalck, J., Mitchell, K., Meng, C. J., Arsenault, K., Cosgrove, B., Radakovich, J., Bosilovich, M., Entin, J. K., Walker, J. P., Lohmann, D., and Toll, D.: The Global Land Data Assimilation System, B. Am. Meteorol. Soc., 85, 381–394, https://doi.org/10.1175/BAMS-85-3-381, 2004.

Rounce, D. R., Hock, R., and Shean, D. E.: Glacier Mass Change in High Mountain Asia Through 2100 Using the Open-Source Python Glacier Evolution Model (PyGEM), Front. Earth Sci., 7, 331, https://doi.org/10.3389/feart.2019.00331, 2020.

Scott, C. A., Zhang, F., Mukherji, A., Immerzeel, W., Mustafa, D., and Bharati, L.: Water in the Hindu Kush Himalaya, in: The Hindu Kush Himalaya Assessment: Mountains, Climate Change, Sustainability and People, edited by: Wester, P., Mishra, A., Mukherji, A., and Shrestha, A. B., Springer International Publishing, Cham, 257–299, 2019.

Sexton, J. O., Song, X.-P., Feng, M., Noojipady, P., Anand, A., Huang, C., Kim, D.-H., Collins, K. M., Channan, S., DiMiceli, C., and Townshend, J. R.: Global, 30-m resolution continuous fields of tree cover: Landsat-based rescaling of MODIS vegetation continuous fields with lidar-based estimates of error, Int. J. Digit. Earth, 6, 427–448, https://doi.org/10.1080/17538947.2013.786146, 2013.

Shean, D. E., Bhushan, S., Montesano, P., Rounce, D. R., Arendt, A., and Osmanoglu, B.: A Systematic, Regional Assessment of High Mountain Asia Glacier Mass Balance, Front. Earth Sci., 7, 363, https://doi.org/10.3389/feart.2019.00363, 2020.

Smith, T. and Bookhagen, B.: Assessing uncertainty and sensor biases in passive microwave data across High Mountain Asia, Remote Sensing of Environment, 181, 174–185, 2016.

Smith, T. and Bookhagen, B.: Changes in seasonal snow water equivalent distribution in High Mountain Asia (1987 to 2009), Sci. Adv., 4, e1701550, https://doi.org/10.1126/sciadv.1701550, 2018.

Smith, T. and Bookhagen, B.: Assessing Multi-Temporal Snow-Volume Trends in High Mountain Asia From 1987 to 2016 Using High-Resolution Passive Microwave Data, Front. Earth Sci., 8, 392, https://doi.org/10.3389/feart.2020.559175, 2020.

Sorg, A., Bolch, T., Stoffel, M., Solomina, O., and Beniston, M.: Climate change impacts on glaciers and runoff in Tien Shan (Central Asia), Nat. Clim. Change, 2, 725–731, 2012.

Stigter, E. E., Wanders, N., Saloranta, T. M., Shea, J. M., Bierkens, M. F. P., and Immerzeel, W. W.: Assimilation of snow cover and snow depth into a snow model to estimate snow water equivalent and snowmelt runoff in a Himalayan catchment, The Cryosphere, 11, 1647–1664, https://doi.org/10.5194/tc-11-1647-2017, 2017.

Sun, S. and Xue, Y.: Implementing a new snow scheme in Simplified Simple Biosphere Model, Adv. Atmos. Sci., 18, 335–354, 2001.

Tahir, A. A., Chevallier, P., Arnaud, Y., and Ahmad, B.: Snow cover dynamics and hydrological regime of the Hunza River basin, Karakoram Range, Northern Pakistan, Hydrol. Earth Syst. Sci., 15, 2275–2290, https://doi.org/10.5194/hess-15-2275-2011, 2011.

Takala, M., Luojus, K., Pulliainen, J., Derksen, C., Lemmetyinen, J., Kärnä, J.-P., Koskinen, J., and Bojkov, B.: Estimating northern hemisphere snow water equivalent for climate research through assimilation of space-borne radiometer data and ground-based measurements, Remote Sens. Environ., 115, 3517–3529, 2011.

Terzago, S., Hardenberg, von, J., Palazzi, E., and Provenzale, A.: Snowpack Changes in the Hindu Kush–Karakoram–Himalaya from CMIP5 Global Climate Models, J. Hydrometeorol., 15, 2293–2313, https://doi.org/10.1175/JHM-D-13-0196.1, 2014.

Wang, X., Wu, C., Wang, H., Gonsamo, A., and Liu, Z.: No evidence of widespread decline of snow cover on the Tibetan Plateau over 2000–2015, Sci. Rep., 7, 14645, https://doi.org/10.1038/s41598-017-15208-9, 2017.

Winiger, M., Gumpert, M., and Yamout, H.: Karakorum-Hindukush-western Himalaya: assessing high-altitude water resources, Hydrol. Process., 19, 2329–2338, https://doi.org/10.1002/hyp.5887, 2005.

Wrzesien, M. L., Pavelsky, T. M., Durand, M. T., Dozier, J., and Lundquist, J. D.: Characterizing Biases in Mountain Snow Accumulation From Global Data Sets, Water Resour. Res., 55, 9873–9891, https://doi.org/10.1029/2019WR025350, 2019.

Xue, Y., Sun, S., Kahan, D. S., and Jiao, Y.: Impact of parameterizations in snow physics and interface processes on the simulation of snow cover and runoff at several cold region sites, J. Geophys. Res., 108, https://doi.org/10.1029/2002JD003174, 2003.

Xue, Y., Houser, P. R., Maggioni, V., Mei, Y., Kumar, S. V., and Yoon, Y.: Assimilation of Satellite-Based Snow Cover and Freeze/Thaw Observations Over High Mountain Asia, Front. Earth Sci., 7, 872, https://doi.org/10.3389/feart.2019.00115, 2019.

Yao, T., Thompson, L., Yang, W., Yu, W., Gao, Y., Guo, X., Yang, X., Duan, K., Zhao, H., Xu, B., Pu, J., Lu, A., Xiang, Y., Kattel, D. B., and Joswiak, D.: Different glacier status with atmospheric circulations in Tibetan Plateau and surroundings, Nat. Clim. Change, 2, 663–667, 2012.